UNIVERSITY OF OKLAHOMA

GRADUATE COLLEGE

RELATIONSHIPS BETWEEN THE CIRCULATION AND EASTWARD PROPAGATION OF THE MADDEN-JULIAN OSCILLATION

A THESIS

SUBMITTED TO THE GRADUATE FACULTY

in partial fulfillment of the requirements for the

Degree of

MASTER OF SCIENCE IN METEOROLOGY

By

ANDREW H. BERRINGTON
Norman, Oklahoma
2020

THE RELATIONSHIP BETWEEN THE CIRCULATION AND PROPAGATION OF THE MADDEN-JULIAN OSCILLATION

A THESIS APPROVED FOR THE
SCHOOL OF METEOROLOGY

BY THE COMMITTEE CONSISTING OF

Dr. Naoko Sakaeda, Chair

Dr. Jason C. Furtado

Dr. Elinor R. Martin

Acknowledgements

I would like to first thank my advisor, Dr. Naoko Sakaeda, for her patience, endless support be it academically or otherwise, commitment to my success, and instruction on techniques necessary to complete both my coursework and this thesis. None of this would have been possible without her. I would also like to thank my committee members, Dr. Jason Furtado and Dr. Elinor Martin, for dedicating their time through suggestions and reviewing of my thesis towards my goal of completing my Masters degree. The former's Advanced Statistics class was also a wonderful resource for multiple methods used in this thesis and I would certainly not be here without it. I'd like to thank Dr. George Kiladis, Dr. Juliana Dias, and Dr. Brandon Wolding at the Earth System Research Lab in Boulder for helpful suggestions that assisted me in streamlining this work. I want to extend my gratitude to my friends here in Norman and back at home in British Columbia, for I'm glad I shared the journey that got me here with you and its comforting to know you have my back, especially during the trying times we've lived in recently. I want to thank my parents and extended family for raising me into the person I've become today. I am endlessly in debt to you all and, again, I would never be in this position without you. Last, but certainly not least, I'd like to acknowledge the National Oceanographic and Atmospheric Administration (NOAA) Climate Office for providing the funding for this research, along with the European Center for Medium-Range Weather Forecasts (ECMWF) and NOAA for providing the data necessary to complete this research.

Table of Contents

List of Figures

Abstract

The Madden-Julian Oscillation (MJO) is the dominant mode of intraseasonal variability in the tropics and represents a major connection between global weather and climate. Successful prediction of the phenomenon has proved to be a great challenge for both operational and climate models. In particular, the propagation of the MJO around the Maritime Continent remains a lingering question, in part due to differing explanations of the fundamental dynamics necessary for propagation across the Maritime Continent.

The circulation response to convection of the MJO has been suggested to have an impact on its propagation by a number of previous studies. This circulation contains both flanking Rossby waves to the rear and a Kelvin wave leading the convective center. In this study, we use a two-dimensional tracking mechanism to follow individual MJO events from a 40-year database, employ a technique to scale the MJO by its zonal wavelength, and use statistical methods to assess the role of the circulation in impacting propagation downstream.

Results suggest that both the geopotential height and wind anomalies east of the convective center are important to the eastward propagation of the MJO, which also changes depending on the region that the MJO is located over. Continuous eastward propagation is favored by having a Kelvin wave circulation, indicated by an easterly zonal wind anomaly and negative geopotential height anomaly east of MJO convection. Kelvin wave circulation east of MJO convection enhances moistening to support continuous eastward propagation of the MJO, mainly through meridional moisture advection. This is in contrast to several previous studies emphasizing the role of the Kelvin circulation in impacting boundary layer moisture convergence and vertical moisture advection. In addition to the known significance of having Kelvin wave easterly wind anomalies, the results of this study highlight that the existence of negative geopotential height is important to supporting moistening and MJO propagation, especially over the Indian Ocean. This thesis provides more insight into the relationships between MJO circulation and propagation by highlighting the sensitivity of MJO propagation to its circulation structure and its interaction with moisture.

1. Introduction

1.1. Observed Characteristics, Significance, and Challenges of the MJO

The phenomenon of a 40 to 50 day zonal wind oscillation in the Tropical Pacific was first described by Roland Madden and Paul Julian in their seminal 1971 paper (Madden and Julian 1971). Hereby referred to as the Madden-Julian Oscillation (MJO), it is the dominant mode of intra-seasonal variability in the tropics on a timescale of 30 to 90 days (Madden and Julian 1972; Madden and Julian 1994; Zhang 2005). The MJO represents a vital connection between weather and climate timescales through its impacts on a broad range of tropical weather and climate such as the Asian Summer Monsoon (Singh et al. 1992; Lawrence and Webster 2002; Chang et al. 2006; Pai et al. 2011), tropical cyclone activity in all of the world's ocean basins (e.g. Liebmann et al. 1994; Ferreira et al. 1996; Maloney and Hartmann 2000; Maloney and Hartmann 2001; Hall et al. 2001; Bessafi and Wheeler 2006; Barrett and Leslie 2009; Klotzbach 2010), and Australian precipitation (Hall et al. 2001; Wheeler et al. 2009). Expanding from the tropics, several works have examined the MJO interactions with extratropical phenomena including the North American Monsoon (Higgins and Shi 2001; Lorenz and Hartmann 2006), Arctic circulation and the Arctic Oscillation (Zhou and Miller 2005; L'Heureux and Higgins 2008; Yoo et al. 2012) and the North Atlantic Oscillation (Cassou 2008; Lin et al. 2009; Henderson et al. 2016). General characteristics of the MJO are summarized as a planetary-scale (zonally spanning tens of thousands of kilometers), organized region of anomalous convection and associated circulation that propagates eastward from the Indian Ocean to at least the Central Pacific at speeds of roughly 5 m s^{-1} (Madden and Julian 1994; Wheeler and Hendon 2004; Kiladis et al. 2005; Zhang 2005). Cloud populations within the MJO evolve from shallow cumulus clouds, cumulus congestus, and then to deep convection with associated stratiform (Benedict and Randall 2007; Riley et al. 2011). The MJO also alters surface pressure and relative atmospheric angular momentum during its passage (Gutzler and Ponte 1990; Madden and Julian 1994; Weickmann et al. 1997). The convective signal of the MJO reaches a peak in amplitude over the Indo-Pacific warm pool and generally decays upon reaching the central-eastern equatorial Pacific (Hendon and Salby 1994; Zhang

2005). Once it moves eastward of the Indo-Pacific warm pool, the circulation signal is reminiscent of a Kelvin wave in its propagation speed that can continue to propagate across the globe (Hendon and Salby 1994; Sobel and Kim 2012).

Despite these global impacts of the MJO, the current operational and global circulation models (GCMs) struggle to capture the fundamental characteristics of the MJO. In particular, understanding the dynamics of MJO propagation is critical to improving the prediction skill of the MJO and its impact on global weather and climate. Forecasting the MJO has been shown to have a substantial effect on medium and extended range prediction across the globe (e.g. Ferranti et al. 1990; Hendon et al. 2000; Lo and Hendon 2000; Waliser et al. 2003; Gottschalck et al. 2010; Kim et al. 2018). Assessment of the prediction skill of the MJO itself has been conducted amongst an assortment of operational numerical (e.g. Waliser et al. 2006; Lin et al. 2008; Seo et al. 2009; Gottschalck et al. 2010; Hamill and Kiladis 2014; Kim et al. 2014; Kim et al. 2016) and general circulation models (D. Kim et al. 2009; Hung et al. 2013; Jiang et al. 2015; Wang and Lee 2017; Lim et al. 2018). One of the key findings from Hamill and Kiladis (2014), using re-forecasts of the Global Ensemble Forecast System (GEFS), was that high amplitude MJO events tended to propagate too slowly in the Indian Ocean compared to observations. The same issue concerning errors in MJO propagation speed was indicated in Vitart and Molteni (2010) and Ling et al. (2014) with the European Centre for Medium- Range Weather Forecasts (ECMWF) forecast system. Wang and Lee (2017) showed that only a small fraction of GCMs within a 24 member-ensemble with the purpose of advancing MJO predictive abilities had reliable skill in forecasting MJO propagation from the Indian Ocean into the West Pacific. A major difficulty in forecasting the MJO has been documented around the region of the Maritime Continent (Vitart and Molteni 2010; Weaver et al. 2011; Fu et al. 2013; Kim et al. 2016; Jiang et al. 2020), where models commonly depict MJO decay to a greater extent than is actually observed (D. Kim et al. 2009; Kerns and Chen 2016; Zhang and Ling 2017). Here, complex terrain affects the circulation of the MJO, the diurnal cycle of its convection, and surface fluxes (Wu and Hsu 2009; Peatman et al. 2014; DeMott et al. 2018; Ling et al. 2019; Ahn et al. 2020) and results in changes in the propagation

characteristics of the MJO (Zhang and Ling 2017; Wang et al. 2019), where some events continue into the West Pacific, while others weaken.

The difficulty in forecasting the MJO can be tied to the lack of a complete theory to explain its fundamental dynamics, such as eastward propagation, phase speed, and the selection of planetary spatial scale. In addition, individual MJO events exhibit a substantial amount of dispersion in evolution and structure (Adames and Wallace 2014a; Wang et al. 2019), while many prior studies often examine the general characteristics of the MJO by compositing multiple events. Such multi-event compositing analyses has revealed several canonical features of the observed MJO, including its westward-tilted baroclinic vertical structure and its horizontal structure that is reminiscent of a coupled Kelvin-Rossby wave response to a tropical heating source (Gill 1980; Rui and Wang 1990; Hendon and Salby 1994; Sperber 2003; Kiladis et al. 2005; Adames and Wallace 2014b; Wang and Chen 2017). General components of this structure are shown in Figure 1, where the convective center of the MJO is located over the Indian Ocean.

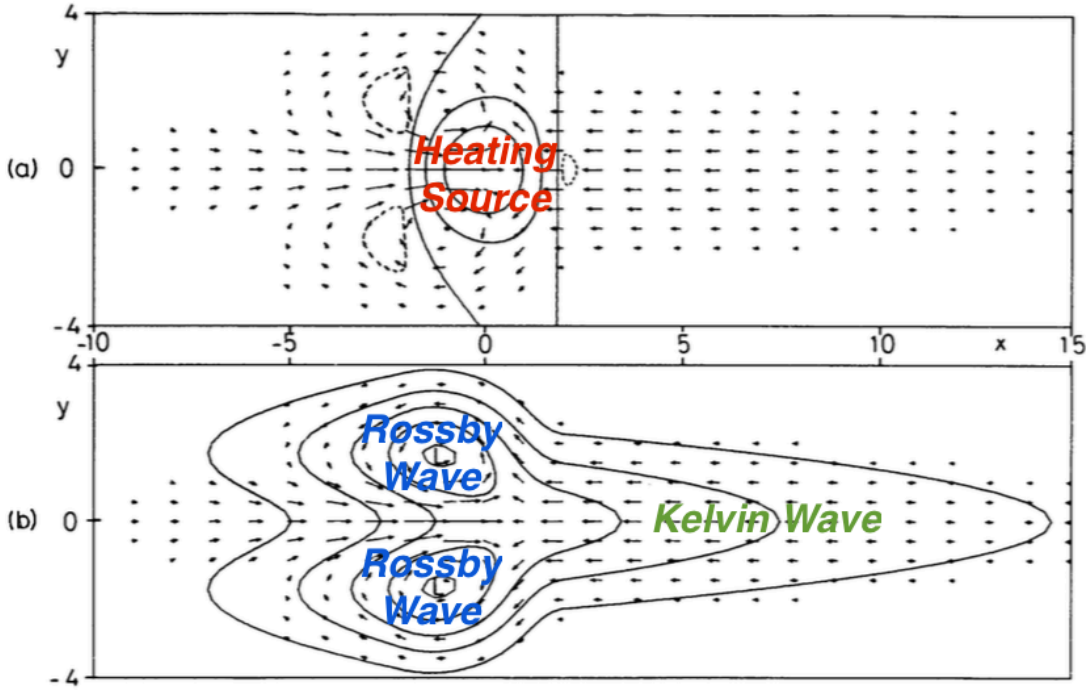

Figure 1: Annotated figure 1a and 1b from Gill (1980) showing the circulation response to a tropical heating source. X-axis is longitude in degrees, Y-axis is latitude in degrees, and vectors are horizontal wind anomalies. Contours in 1a represent anomalous heating, and contours in 1b represent negative pressure anomalies.

Leading the convective center in the low levels, anomalous low pressure straddles the equator in the form of a Kelvin wave, accompanied by boundary layer moisture convergence. Trailing the convective center are flanking Rossby wave on either side of the equator, with overturning vertical circulations both downstream and upstream of the convection. It is important to note that the definition of 'Kelvin' or 'Rossby' circulation differs from Matsuno (1966) or Gill (1980) when examining the MJO. Namely, the winds for the MJO are presented in the form of filtered anomalies relative to climatology, rather than absolute westerlies or easterlies. The work of Gill (1980) also assumes a background state at rest, which is not present in the real atmosphere. For these reasons, we refrain from referring to the circulation responses detailed throughout this study as "Gill circulations".

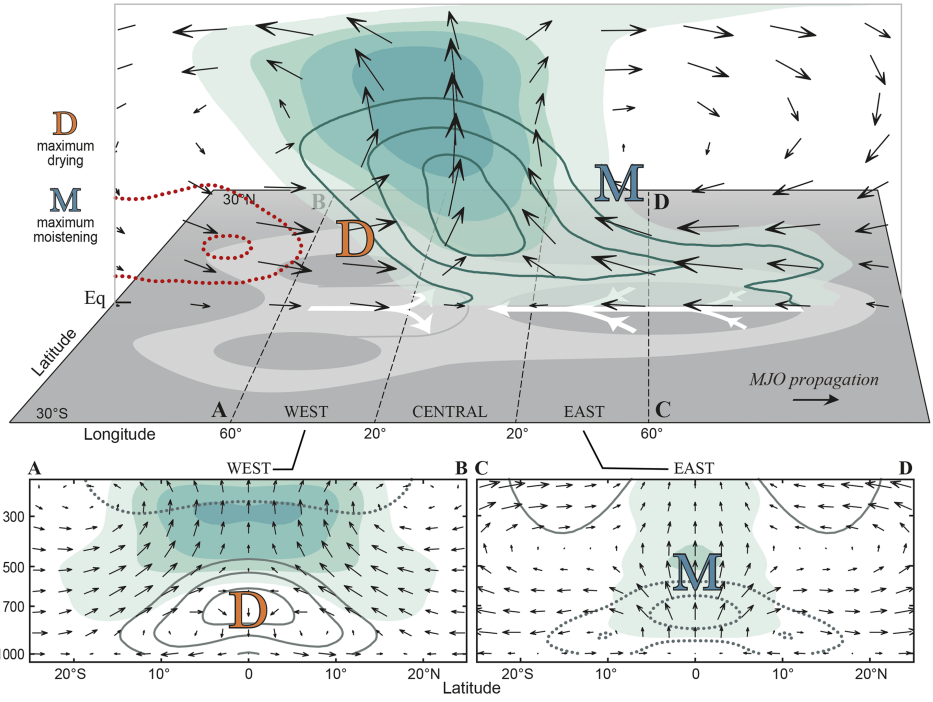

Figure 2: Figure 16 from Adames and Wallace (2015) depicting the three-dimensional circulation structure of the MJO over the Maritime Continent and its interaction with the moisture field. Specific humidity (contours), relative humidity (shaded), and zonal mass circulation (black arrows) are plotted, with M and D corresponding to the regions of maximum moistening and drying, respectively.

The interactions between the observed circulation and moisture are thought to be important to MJO dynamics. Figure 2 summarizes the three dimensional circulation of

the MJO and its interaction with the moisture field over the Maritime Continent as it propagates eastward. Observations from various combinations of reanalysis, radiosonde, and satellite data also indicate that anomalous boundary layer moisture convergence tends to exist to the east of the MJO's convective center (Madden and Julian 1972; Hendon and Salby 1994; Kiladis et al. 2005; Adames and Wallace 2015). Deepening of the moist boundary layer (Kembell-Cook and Weare 2001; Johnson and Ciesielski 2017), a build-up of convective instability (Hsu and Li 2012), poleward flow in the lower free troposphere leading to positive moisture advection away from the mean moisture gradient (Wolding and Maloney 2015), and cloud populations transitioning from shallow cumulus to deep convection and associated anvil stratiform regions (Benedict and Randall 2007; Virts and Wallace 2010; Riley et al. 2011; Rowe and Houze 2015) are also present to the east of the MJO's convective center. The presence of all of these features eastward of the convective center suggests that they all may have some role in determining propagation characteristics. The theoretical models summarized below tend to incorporate some of these fundamental structures and their interactions with the broader environment.

1.2. Existing Theory of MJO Dynamics

Several hypotheses have emerged aiming to explain both the MJO's existence and its observed characteristics. These theories primarily use simplified models of the tropical atmosphere to attempt to capture key processes that result in the eastward propagation and planetary scale of the MJO. The recent review of MJO dynamics by Zhang et al. (2020) discussed two theories of the MJO – the "moisture mode" and "trio-interaction" models that will be summarized here.

The so-called "moisture mode", or moisture-wave model, considers moisture as the most important prognostic variable to MJO dynamics (Yu and Neelin 1994; Raymond and Fuchs 2009; Kiranmayi and Maloney 2011; Sobel and Maloney 2012, 2013; Pritchard and Bretherton 2014; Adames and Kim 2016; Wolding et al. 2016; Jiang 2017). Under the weak temperature gradient (WTG) approximation (Sobel et al. 2001), the organization and maintenance of the MJO's convectively active region is

strongly associated with column moisture and moist static energy (MSE) anomalies. Therefore, budget analysis of column-integrated MSE is often used to study MJO dynamics (e.g. Maloney 2009; Kiranmayi and Maloney 2011; Sobel and Maloney 2012; D. Kim et al. 2014; Jiang et al. 2015; L. Wang et al. 2017). The propagation of the MJO under this framework can be understood through processes that lead to eastward propagation of intraseasonal MSE anomalies such as moisture advection, surface fluxes, and cloud-radiative feedback. Adames and Kim (2016) suggested that both the Kelvin and Rossby circulations contribute to increasing MSE anomalies eastward of MJO convection, contributing to its eastward propagation through destabilization and subsequent convective development.

In Wang and Rui (1990), the MJO was proposed to be a coupled Rossby-Kelvin mode that has its largest growth rate at the planetary scale. Coupling of the Rossby-Kelvin wave structure of the disturbance is a result of frictional convergence. More recent studies have closely examined the role of the Rossby-Kelvin asymmetric structure in determining eastward propagation and its influence on the moisture field (e.g. Hsu and Li 2012; Wang and Lee 2017). In the so-called "trio-interaction" model (Wang et al. 2016; Wang and Chen 2017; Chen and Wang 2019), the relationship between moisture, convective diabatic heating, and dynamics (both related to waves and boundary layer flow) is emphasized and acts as an extension to the Matsuno (1966)-Gill (1980) response to a tropical heating source. Cumulus parameterization schemes are important in this framework and in the moisture mode framework, as the relationship between shallow convective heating and boundary layer convergence influences propagation and organization of the coupled Rossby-Kelvin wave components. A series of modeling experiments (e.g. L. Wang et al. 2017; Wang and Lee 2017; Wang et al. 2018; L. Wang et al. 2018) assessing the role of the interaction between the Rossby-Kelvin asymmetric structure and the moisture field in an ensemble of climate models from the MJO Task Force/GEWEX Atmosphere System Study (GASS) followed. Wang et al. (2018) developed a set of dynamically oriented diagnostics aimed at assessing the skill of the climate models in the ensemble to simulate the eastward propagation of the MJO. Considerable skill was noted in simulating MJO propagation when the models better represented features such as the equatorial vertical structure of diabatic heating,

available potential energy generation, and the horizontal arrangement of boundary layer moisture convergence. Therefore, there may be significance in these features in determining propagation characteristics. These diagnostics are not necessarily independent.

1.3. Observational and Modeling Studies of MJO Propagation Dynamics

In three separate studies addressing propagating versus non-propagating MJO events (those which propagate across the Maritime Continent versus those that do not), D. Kim et al. (2014), Feng et al. (2015), and Chen and Wang (2018) found differing processes driving or impeding propagation beyond the Maritime Continent. D. Kim et al. (2014) found that the existence of a suppressed convective envelope ahead of the MJO enhanced convective envelope is important for the MJO to continue propagating. The schematic in Figure 3 shows this interaction.

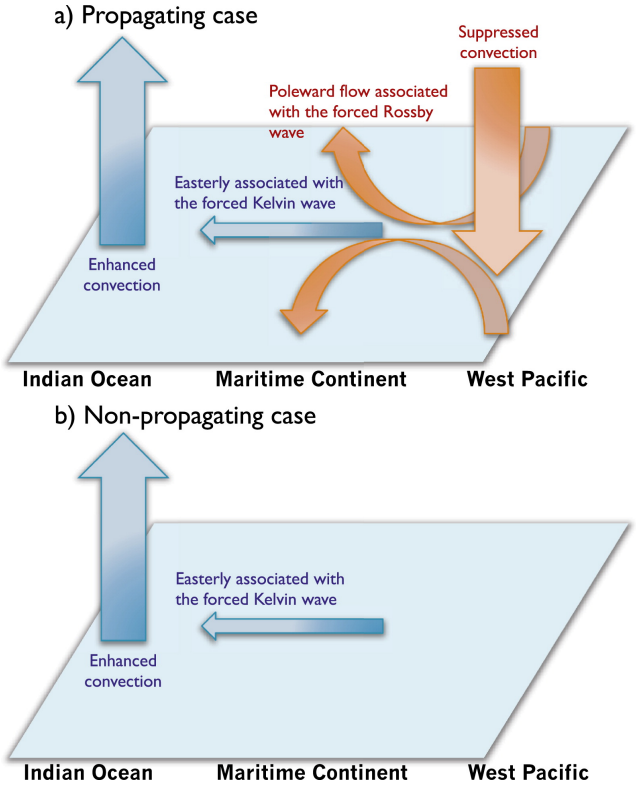

Figure 3: Figure 15 from Kim et al. (2014) depicting the differences in their studies between (a) MJO events that do propagate and (b) MJO events that do not propagate across the Maritime Continent.

A Rossby wave response to the negative heating anomaly associated with the convectively suppressed region drives poleward meridional wind anomalies that lead to anomalous lower tropospheric moistening eastward of MJO enhanced convection, which is not present in the non-propagating cases. Since the Kelvin wave response to the convectively active region is relatively similar in both cases, its importance in delineating between propagating and non-propagating cases is less emphasized in this particular study. Pritchard and Bretherton (2014) found that artificially increasing the rotational component (i.e., by tropical vorticity anomalies) to the moisture advection leads to amplification, increases in phase speed, and further eastward propagation of their modeled MJO.

Chen and Wang (2018) also determined that a leading suppressed convective region was a strong precursor signal for propagation. In their work, a robust suppressed convective region resulted in an intensification of the circulation cell downstream of the convective center. The suppressed convective region itself was a result of either a proceeding MJO-related dry phase propagating eastward into the West Pacific, or a two-way interaction between preceding Indian Ocean suppressed convection and a tropical-extratropical teleconnection that generates a western North Pacific cyclone in the upper levels. In these cases, the western North Pacific extratropical cyclone induces upper level convergence over the western tropical Pacific and thereby strengthens the suppressed convective region. Increasing the magnitude of the forward Walker cell leads to stronger boundary layer convergence, more cumulus convection and pre-conditioning, and triggering of new deep convection downstream of the convective center.

Meanwhile, Feng et al. (2015) found that westward-propagating Rossby waves in the equatorial Pacific, independent of the MJO, lead to dry air intrusion ahead of the convectively active region, which then hinders convective development downstream of the convective center and halts propagation. Meridional advection of background mean MSE was not significantly affected by the strength of the leading convectively suppressed region, contrasting with D. Kim et al. (2014). Findings from DeMott et al. (2018) suggest a similar mechanism for MJO decay over the Maritime Continent in some cases. Feng et al. (2015) also determined a dichotomy of moistening processes in

the propagating cases, which challenges the notion from D. Kim et al. (2014) that a convectively suppressed (dry) anomaly is necessary for propagation across the Maritime Continent. In cases where there was a substantial convectively suppressed region ahead of the convective center, horizontal moisture advection through both intraseasonal and higher frequency wind anomalies is the dominant process. However, in propagating cases without a strong suppressed region leading the convective center, anomalous vertical moisture advection is the dominant process.

In addition to the studies discussed above, Hsu and Li (2012) examined the significance of boundary layer moisture asymmetry enforced by the coupled Rossby-Kelvin wave structure of the MJO for effects on propagation across different longitude regions. Dominant terms in their moisture budget analysis were vertical advection and horizontal moisture convergence due to advection by the MJO's horizontal winds. Boundary layer convergence ahead of the convective center is seen as crucial in driving the stepwise convective evolution seen with the MJO. Most of this boundary layer convergence is associated with the Kelvin wave response to the east of the convective center, and therefore the strength of the Kelvin wave response may be seen as important in determining propagation characteristics. These studies postulate that the key elements to propagation are moistening processes associated with the Rossby-Kelvin wave circulation of the MJO. However, they do not agree on what is the dominant moistening process that is key to MJO eastward propagation, diverging amongst the horizontal advection, mid-tropospheric vertical advection, and shallow moistening through boundary layer convergence.

The diversity of MJO propagation was further tested by Wang et al. (2019), who postulated that the primary mechanism in establishing propagation across the Maritime Continent of MJO events centered in the eastern Indian Ocean was the strength of the Kelvin wave response driving frictional boundary layer moisture convergence ahead of the convective center. Vertical cross sections also suggested that anomalous descending motion to the east of the convective center, partly associated with the Kelvin response, can decrease mid tropospheric MSE and increase destabilization of the lower troposphere, favoring stronger convection and preconditioning. Speed of propagation is also influenced by the Kelvin response's strength and zonal extent, with faster

propagation occurring with a higher amplitude and longer Kelvin response. Impacts of ENSO on the Kelvin response suggest that faster propagation may occur during El Nino as opposed to La Nina, where the coupling of convection and the Kelvin response is stronger and weaker, respectively. Jiang et al. (2015) found that correctly simulating the Kelvin wave component in a set of GCMs was crucial in establishing prediction skill of the MJO's propagation. Gonzalez and Jiang (2017) used the same ensemble of GCMs and suggested that adequately depicting the mean moisture field over the Maritime Continent was crucial for forecasting the MJO's propagation.

1.4. Objective of this Study

To improve our understanding of how the Kelvin-Rossby circulation components play a role in MJO propagation, this study seeks to identify MJO circulation structure and examine its effects on propagation. Prior methodologies for identifying Kelvin and Rossby circulation components contain uncertainty, which might have led to the disagreement of MJO propagation mechanism among the prior studies. We aim to eliminate such ambiguity of the mechanism behind the variance of MJO propagation extent using observational and reanalysis data. Namely, are the properties of the MJO's convection and its circulation itself important for propagation? This is partially motivated by the conflicting results of recent studies regarding the MJO's coupled Kelvin-Rossby wave structure and which component drives its eastward propagation (e.g. L. Wang et al. 2017; Wang et al. 2019). A new object-oriented tracking mechanism to follow MJO convective envelopes in the OLR data will be used, in order to avoid some of the shortcomings of methods such as the Real-time Multivariate MJO Index (RMM) or the OLR MJO Index (OMI) (Straub 2013; Kiladis et al. 2014). Particular attention will be paid to answering three points:

1) How does the zonally asymmetric structure of the MJO changes as the convective envelope propagates?
2) Does MJO circulation structure have significant consequences on whether the MJO propagates across the Maritime Continent?

3) Through which mechanism does MJO circulation support the eastward propagation of its convection across the Maritime Continent?

Chapter 2 will outline the data and methods necessary for tracking the MJO in two dimensions (latitude and longitude) and present some initial results comparing inter-annual (e.g. the El Nino-Southern Oscillation; ENSO and Quasi-Biennial Oscillation; QBO) and convective (MJO convection amplitude and zonal width) variability and effects on propagation. A presentation of the data and methods for measuring the strength of the Rossby-Kelvin components of the circulation and their effects on MJO propagation is given in Chapter 3. Chapter 4 assesses the physical implications behind the results found in Chapter 3, mostly through interaction with the moisture field. In the final chapter, we present a discussion and summary of the results and what they may suggest for future study of the propagation mechanisms of the MJO.

2. Tracking of MJO Propagation and its Variability

This chapter describes an algorithm to track MJO convection using OLR and demonstrates event-by-event variability of MJO propagation characteristics. One of the questions regarding propagation is whether climate variability has a substantial effect. A number of studies have tied behavior of the MJO to such variability as the QBO (Yoo and Son 2016; Marshall et al. 2017; Nishimoto and Yoden 2017; Zhang and Zhang 2018) and ENSO (Moon et al. 2011; Wei and Ren 2019). If we can find statistically significant results between different states of interannual climate variability, it may provide additional insight into what is ultimately controlling the variability in propagation extents. For example, if warmer sea surface temperature anomalies over the western Pacific are favored with a corresponding positive ENSO phase, it may suggest that eastward extension to the Indo-Pacific warm pool leads to an increased chance of propagation through various processes. A number of previous studies (Yoo and Son 2016; Son et al. 2017; Marshall et al. 2017) suggested a relationship between amplitude of the MJO and QBO phase during boreal winter, with higher amplitude events taking place preferentially under easterly QBO conditions. In this chapter, we aim to use the two-dimensional OLR tracking mechanism to look for differences in MJO event behavior between both interannual variability (outside convective characteristics of the MJO itself), with the goal of determining whether one or the other (or both) need to be scrutinized further in subsequent chapters.

2.1. Data/Methods

2.1a. Tracking Algorithm

To track latitude and longitude locations of both convectively enhanced and suppressed phases of the MJO, we use NOAA Interpolated Daily OLR (Liebmann and Smith 1996) on a 2.5˚ by 2.5˚ horizontal grid (sufficient for planetary scale disturbances such as the MJO) and during the period of 1979–2018. The OLR is filtered for the MJO using the Wheeler and Kiladis (1999) method, which takes the inverse of Fourier

coefficients including only intraseasonal periods of 20–100 days and eastward zonal wavenumbers 1–10 after removing the mean and first three harmonics of the seasonal cycle. This study only examines MJO events that occur during the period from November to March to separate the events from the Boreal Summer Intraseasonal Oscillation, which exhibits significantly different characteristics to its boreal winter counterpart (Lawrence and Webster 2002). We use the MJO-filtered OLR anomalies to identify and track MJO convective envelopes through the algorithms that extend from Kerns and Chen (2016) and Dias et al. (2017), which is as follows:

I. On each day, spatially continuous regions of MJO-filtered OLR anomaly above or below its upper and lower 15th percentile values within 15˚S–15˚N from 1979–2018 are identified as convectively suppressed and enhanced envelopes of the MJO, respectively. The 15^{th} percentile is close to the highlighted threshold of the daily standard deviation of MJO-filtered OLR documented in Kiladis et al. 2005 (their Figure 1). We will refer to them as MJO "blobs".

II. If a blob overlaps horizontally with a blob in the next day, it is identified as the same blob and its propagation is tracked as an "event".

III. When a single blob splits into two separate blobs in the subsequent time-step, the blob that overlaps more in horizontal space with the original blob is maintained as the same event, while the blob with less horizontal overlap initiates a new event in the tracking algorithm. When two blobs merge into a single blob in the subsequent time-step, the blob that had a larger horizontal overlap with the merged blob is maintained as the same event, while the other with less horizontal overlap is terminated by the algorithm.

IV. Latitude and longitude centroids of the blobs are computed using the absolute values of the filtered OLR anomalies. The blobs are terminated when their centroid moves poleward of the 15˚S–15˚N latitude band.

Among all the identified blobs, we only analyze events that last more than 5 days. We also only include events that have passed through or initiated over the Indian Ocean (45˚E–95˚E) to examine factors that influence MJO propagation across the Maritime Continent. Blob amplitudes are recorded through the spatially averaged OLR anomalies within the blob for each time-step. The zonal width of the blob at each time-step is also computed as the average of its west–east extent at every latitude, weighted by the absolute values of the mean OLR anomalies within the zonal width at each latitude. Both propagation extent through the horizontal displacement between time-steps of the centroids and propagation speed via the temporal duration and zonal extent of the blobs are monitored.

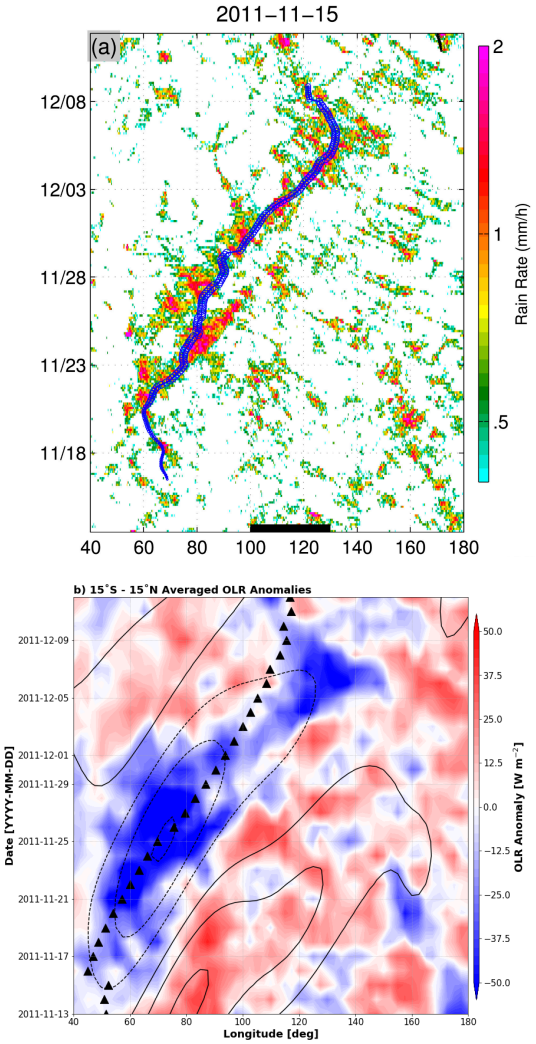

Figure 4: (a) Figure 5a from Kerns and Chen (2016). (b) Hovmoller diagram of seasonal cycle-removed OLR anomalies (shaded in W m^{-2}) with MJO filtered OLR (contours in 10 W m^{-2} intervals) and the longitude centroid (triangle markers) of the DYNAMO MJO event in Nov-Dec 2011.

To demonstrate the validity of the two-dimensional OLR tracking mechanism for examining individual MJO events, a comparison using a well-documented MJO case between the precipitation-based method of Kerns and Chen (2016) and our OLR-based method is presented in Figure 4. Some degree of deviation in the tracks of the centroids is expected given the tendency for OLR anomalies to deviate south of the equator.

The Kerns and Chen method cannot detect convectively suppressed regions or non-precipitating regions. Therefore, we will use the convectively active phase of the middle November – early December 2011 MJO event that was documented by the Dynamics of the MJO (DYNAMO, Gottschalck et al. 2013) field campaign to compare. This particular event was of the highest amplitude documented during the campaign.

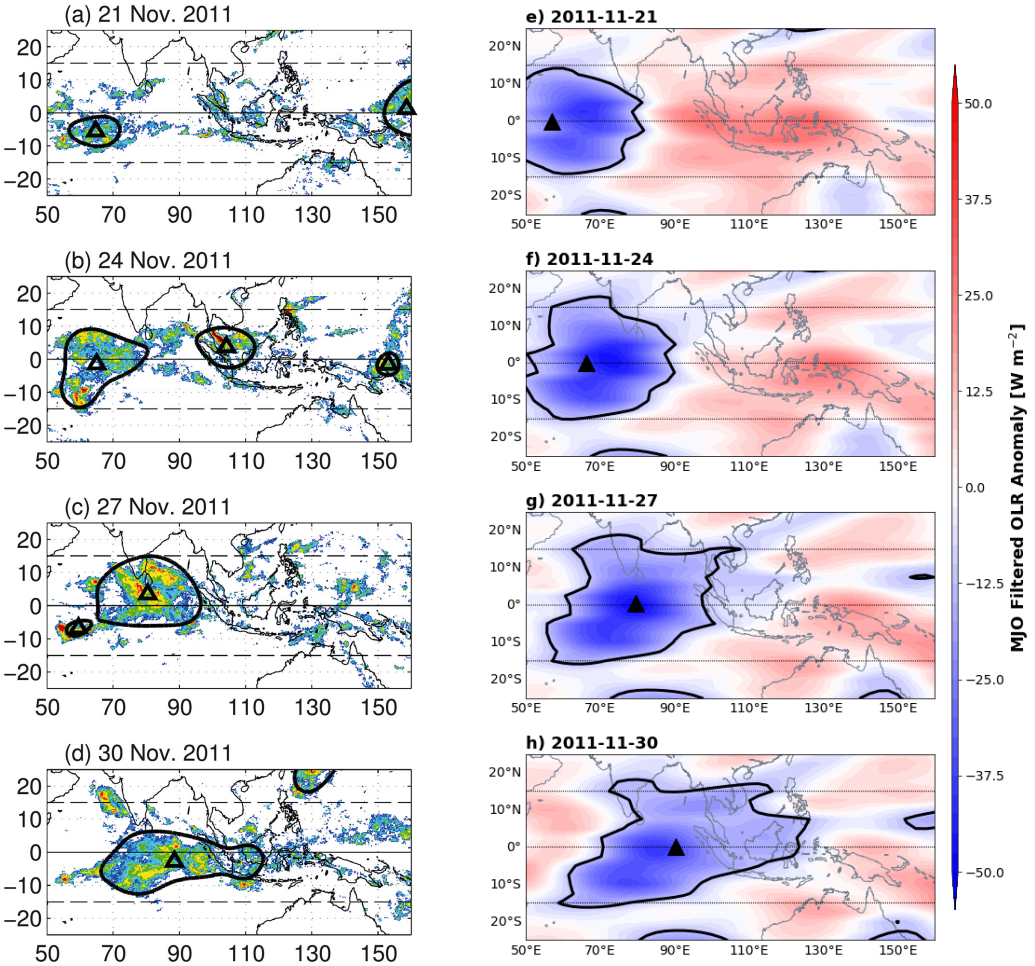

Figure 5: (a)-(d) Figure 3, panels (a)-(d) from Kerns and Chen (2016) for the period from 21 Nov – 30 Nov 2011. (e)-(h) Data from same times for our OLR tracking method over the region from 25˚S – 25˚N and 50˚E – 160˚E. Color shading is MJO filtered OLR anomalies (W m^{-2}), the black triangles represent the latitude and longitude centroids of the identified MJO event at the given time, and the black contours are the -12.5 W m^{-2} isolines.

The Hovmoller diagrams of the OLR-based tracking method compares favorably with the precipitation-based method for this particular case through the period from 15 November through 8 December, showing similar propagation behavior, centroid location, and timing of peak amplitude during the week of 22-29 November. The two methods begin to diverge following the first week of December, with the precipitation algorithm terminating the event and the OLR method continuing the event in a disjointed manner. As negative OLR' (the prime symbol indicating non-standardized anomalies) can still be yielded in cases with minimal precipitation (non-precipitating clouds), in addition to the differences in the handling of splits and thresholds set for termination between the two methods, these types of deviations are to be expected, especially when looking at individual cases. Still, the similarity in the handling of the event during its strongest and most coherent signal yields confidence in using the OLR-based tracking algorithm to examine other events in the period of record with higher scrutiny. A spatial comparison in latitude/longitude space is also provided in Figure 5 to show the two-dimensional assessment between four separate days in late November 2011 and yield further confidence in the OLR method. Latitude/longitude centroids follow similar paths through both, with some expected discrepancies in blob shape and extent given negative OLR' capturing both precipitating and non-precipitating clouds.

2.1b. Indices for Climate Variability and MJO Convective Characteristics

To examine the effects of interannual variability on MJO propagation, monthly ERSSTv5 (Huang et al. 2017) is used to calculate the monthly Oceanic Nino Index (ONI) (Trenberth and Stepaniak 2001) through Nino 3.4 sea surface temperature anomalies (ONI data provided by the NOAA Climate Prediction Center). Monthly QBO index is yielded through the method of Yoo and Son (2016), using ERA-Interim (Dee et al. 2011) zonal mean zonal wind at 50 hPa averaged between 10˚S–10˚N. Warm and cold phases of ENSO are defined as Nino 3.4 index greater than or equal to 0.5 and less than or equal to −0.5 standard deviations, respectively. The positive and negative values of the QBO index represent westerly and easterly zonal wind anomalies, respectively.

Other factors that may influence MJO propagation are the convective amplitude and zonal width of the MJO when it is over the Indian Ocean. The amplitude and zonal

widths of MJO convection over the Indian Ocean are defined as, respectively, the spatially averaged amplitude and zonal widths of the MJO event at the first timestep where it exists between 45–95˚E. We then compute standardized anomalies of both of these convective variabilities and define positive and negative phases similarly to the QBO and ENSO indices above.

Testing the effects of both interannual variability and convective variability on MJO propagation is performed via probability densities of blob termination longitudes between the positive and negative states of each mode of variability. Significance testing is performed using 5000 iterations of a Monte-Carlo resampling test with repetitions at the 95% confidence level.

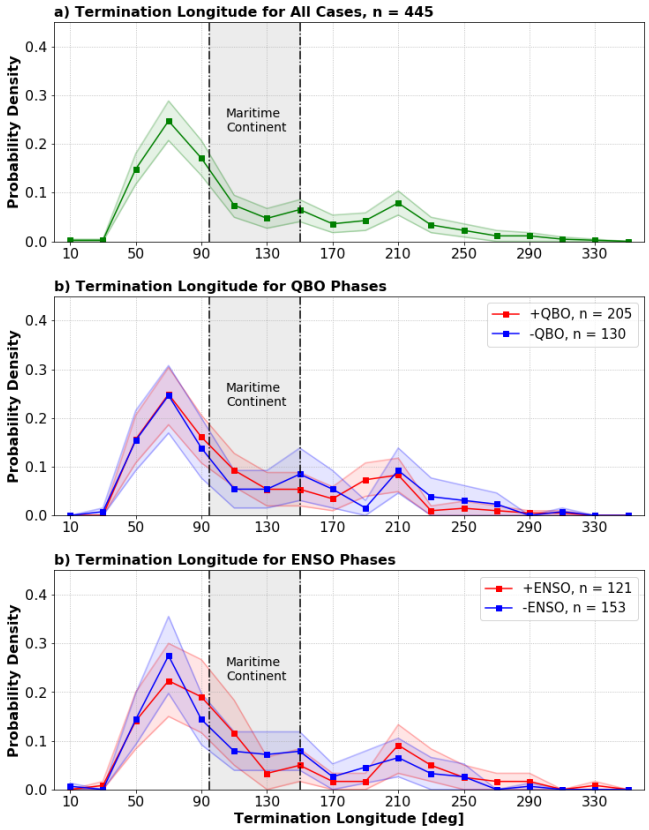

Figure 6: Probability density of negative OLR blob termination longitude (deg E) for (a) all cases; (b) positive or negative QBO phases; (c) positive or negative ENSO phases. Solid lines with markers are actual distributions and shaded regions are 95% confidence intervals. Bin size is 20 degrees and markers are plotted at the bin centers.

2.2. Results

Figure 6 shows the probability distribution functions of longitudes where MJO

enhanced convective envelopes terminate for all events and for events during positive and negative phases of ENSO and the QBO. As mentioned above, termination is defined as when the amplitude of the OLR' in the MJO convective envelope decreases sufficiently (below 15th percentile), or if the centroid of the envelope tracks outside of the tropics. The majority of events in both distributions terminate over the Indian Ocean, indicating that many of them are short-lived or short-tracked. This can be attributed to either inconsistencies in tracking mechanism (such as mergers and splits), or simply that many MJO events do not propagate eastward of the Indian Ocean. Considerable overlap of termination longitude of MJO events in the November–March period between opposite phases of ENSO and QBO indicate that there is little statistical significance for these modes of interannual variability in determining propagation extent. Previous studies such as Wei and Ren (2019) and Wang et al. (2019) discussed the modulation of ENSO on propagation speed of the MJO and agreed that El Nino conditions generally favored faster propagation. However, Wang et al. (2019) separated cases into both slow and fast propagating modes across the Maritime Continent (their Figure 5) and found that sea surface temperature anomalies in the equatorial Pacific resembled cold-neutral or weak La Nina for the slow propagating cases. As we are testing the eastward extent of propagation versus propagation speed, it isn't necessarily surprising to find a lack of significance between ENSO states. Wei and Ren (2019) also found that the MJO tended to detour southward of the Maritime Continent more frequently during cold ENSO, while propagation during warm ENSO was more equatorially symmetric. Neither of these conditions directly suggests a preference towards further propagation, but they may be affected by mean states of moisture near the Maritime Continent (D. Kim et al. 2017).

For the QBO, our result contradicts the results of Zhang and Zhang (2018) and Nishimoto and Yoden (2017), who found differences in MJO propagation during QBO easterly and westerly phases. Our results remain the same even when we limit the analysis to MJO events during December through February, when the relationship between MJO and QBO has been documented. The differing results may be a result of MJO tracking methods differing between the studies. Zhang and Zhang (2018) used precipitation as their variable, while Nishimoto and Yoden (2017) used OMI (Kiladis et

al. 2014). The criteria for what defines an MJO event also differ between the studies. While we find no significance in the relationship between MJO termination longitude and QBO phase, we found higher amplitude MJO events during easterly QBO than westerly QBO in the boreal winter months (not shown) that agrees with previous studies such as Yoo and Son (2016). Hendon and Abhik (2018) and Martin et al. (2019) suggest that this link may be related to temperatures within the tropical tropopause layer (TTL) between easterly and westerly QBO, but our results suggest that this mechanism does not seem to apply to enhancing MJO propagation across the Maritime Continent.

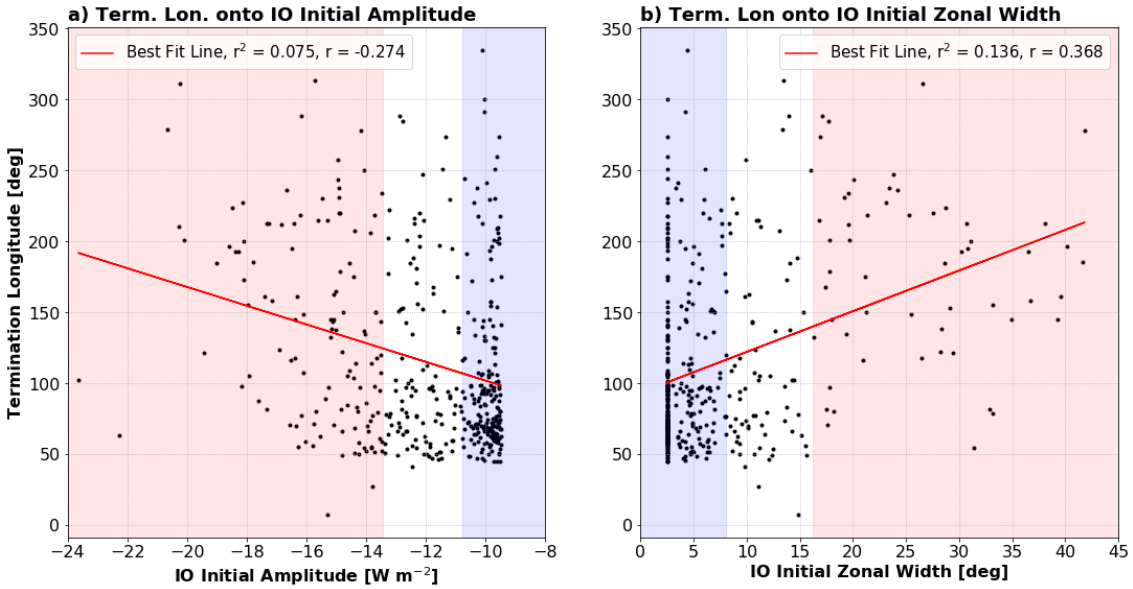

Figure 7: Standard linear regressions and scatter of termination longitude (deg E) onto (a) initial Indian Ocean amplitudes (W m^{-2}) and (b) initial Indian Ocean zonal widths (deg) of MJO convective OLR anomalies. Solid red line represents the best-fit line for each regression. Red shaded region represents a $\geq +0.5$ standardized anomaly and blue shaded region represents a ≤ -0.5 standardized anomaly for each x-variable.

However, when looking at convective variability of the MJO itself in the same manner as the interannual variability, there are some differences in the probability of propagation. Figure 7 shows the scatter of termination longitudes versus initial Indian Ocean amplitude and initial Indian Ocean zonal width. We note some degree of boundary effects to the regression given the threshold of the 15th percentile OLR anomalies, which is slightly lower than –9 W m^{-2}. The correlations for termination longitude versus initial Indian Ocean amplitude and initial Indian Ocean zonal width,

respectively, are –0.274 and 0.368, which are statistically significantly different at the 95% level from zero, indicating modest linear relationships of termination longitude with increasing amplitude (decreasing OLR') and increasing zonal width. However, the amount of spread is considerable at any given amplitude or zonal width, and the correlation coefficients indicate a low percentage of variance explained by initial convective characteristics alone and a relatively poor fit of the linear regression. Neither of the corresponding r^2 values is particularly large. This is to be expected, as the initial state of the MJO in either amplitude or zonal width over the Indian Ocean does not give enough information about how it evolves downstream dynamically, especially given less homogeneous conditions in the boundary layer once the complex terrain of the Maritime Continent becomes involved.

Despite the weak linear relationship between the initial states of the MJO and its termination longitude, the results of the probability density analysis spur further scrutiny into how the convective factors affect the likelihood of propagation across the Maritime Continent. These results motivate further analysis in subsequent chapters that examine what factors influence MJO propagation across the Maritime Continent. Interest rises not only from how the structure of the MJO may impact its propagation into downstream regions, but also how the structure itself changes as it moves into these downstream regions. The MJO circulation pattern is of particular focus, as its interactions with the moisture field are thought to be important in driving destabilization ahead of the convective center in a number of previous studies (e.g. Maloney 2009; Hsu and Li 2012; Sobel and Maloney 2013; Adames and Wallace 2015; DeMott et al. 2018), encouraging propagation. With the help of the two-dimensional OLR tracking mechanism, we can now examine the circulation for individual events and conduct further investigations into its role in driving propagation.

3. The Rossby/Kelvin Circulation and its Relationship with MJO Propagation

3.1. Background

As previously discussed in Chapter 1, the MJO is consistently depicted in composite means as having an anomalous circulation pattern analogous to the response to a tropical heating source (Gill 1980). For MJO convection centered near the equator, this response consists of a pair of flanking equatorial Rossby waves and anomalous equatorial westerly winds near the equator west of the convective signal, and a Kelvin wave centered about the equator east of the convection with anomalous easterly winds.

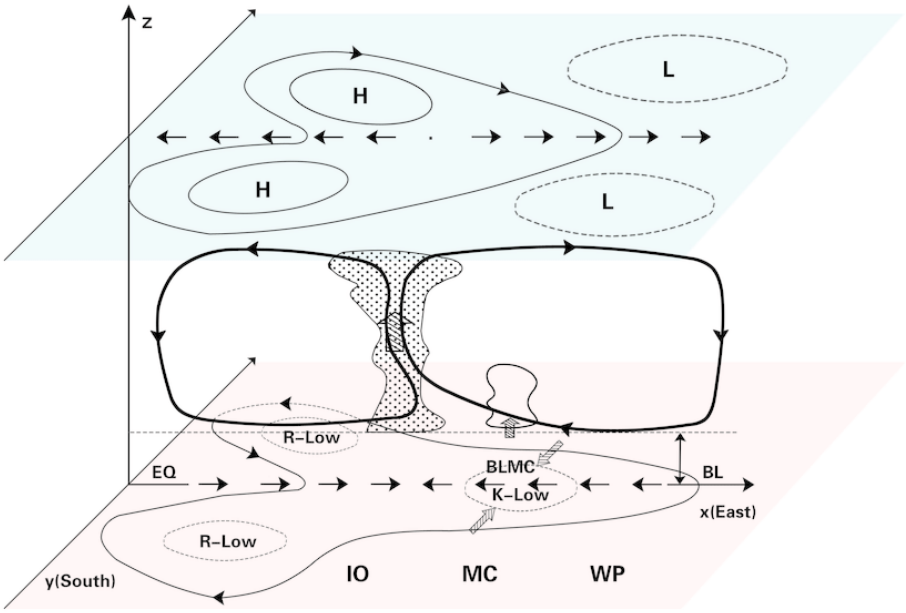

Figure 8: Figure 1 from Wang et al. 2016 showing the three-dimensional circulation surrounding the active convection associated with MJO over the Indian Ocean (IO). Red shading indicates the z-plane near the surface, while blue-green shading indicates the z-plane in the upper troposphere. 'R' indicates Rossby waves and 'K' indicates Kelvin waves. Arrows indicate the direction of mean flow.

Figure 8, as in Wang et al. (2016), depicts the circulation associated with the active convective region of the MJO and some of the associated physical processes. Various studies have attempted to link these circulation structures with propagation of

the MJO (e.g. Hsu and Li 2012; Feng et al. 2015; Wang and Lee 2017; Chen and Wang 2018; Wang et al. 2019). However, a precise method to separate and measure the strength of the Rossby and Kelvin components has not been settled upon in the literature. For example, previous modeling studies have focused on the ratio or sum of the strength of the easterlies ahead of the MJO convection and the westerlies behind the MJO convection when trying to quantify the circulation response (Wang and Lee 2017; L. Wang et al. 2018). Zonal wind anomalies alone do not indicate whether the wind signal is associated with Kelvin or Rossby waves. The theoretical structure of a Kelvin wave from Matsuno (1966) shows that equatorial easterlies occur in the region of negative pressure or geopotential height, while the equatorial easterlies of equatorial Rossby waves occur in the region of positive pressure or geopotential height. Therefore, both the strength of zonal wind anomalies and geopotential height anomalies will be used to identify the existence of Kelvin and equatorial Rossby waves. With the ability of the new tracking mechanism described in Chapter 2 to follow individual MJO events, the objective of this chapter is to assess the effects of the circulation on MJO propagation across different regions of longitude.

3.2. Data/Methods

3.2a. Coordinate Transformation

Previous studies have often computed composites of MJO signals in standard latitude-longitude coordinates. Since MJO convection appears with a range of zonal wavenumbers, individual events may contain different zonal scales. When composited together, this may, depending on the distributions of amplitude and zonal scales amongst the events, generate biases in the results towards certain types of events. We may also assume that the zonal extent of MJO circulation scales with the zonal extent of the convection itself, as suggested by Wang et al. (2019) and Chen and Wang (2020). In this case, a quantification of Kelvin and Rossby circulation of the MJO must also be done according to the zonal scale of MJO convection. The modeling study of L. Wang et al. (2018) used a fixed latitude-longitude box to quantify the response of different variables within the Rossby and Kelvin regions, but this method does not account for

the changing zonal scales between individual MJO events and would feasibly change the results in a multi-event composite, even when the actual magnitude of the circulations are similar.

In order to yield more objective comparisons between individual MJO events, we scale individual events by the zonal extents of MJO convection through a coordinate transformation. This is completed prior to calculating composite means or other analysis. To do this, we define a "zonal phase" angle (θ) as

$$\theta = tan^{-1}\left(\frac{OLR^*}{\left[\frac{dOLR}{dx}\right]^*}\right) \qquad \text{(Eq. 3.1)}$$

where OLR* represents the standardized anomaly of MJO-filtered OLR, averaged from 5 degrees north to south of the latitude of the MJO convective envelope, and [d(OLR)/dx]* is the standardized anomaly of the zonal gradient of the OLR*. Both the OLR anomaly and its zonal gradient are standardized using their climatological standard deviations between 15°N and 15°S prior to calculation. Similar methods were undertaken in Riley et al. (2011) and Sakaeda et al. (2020) in the time dimension.

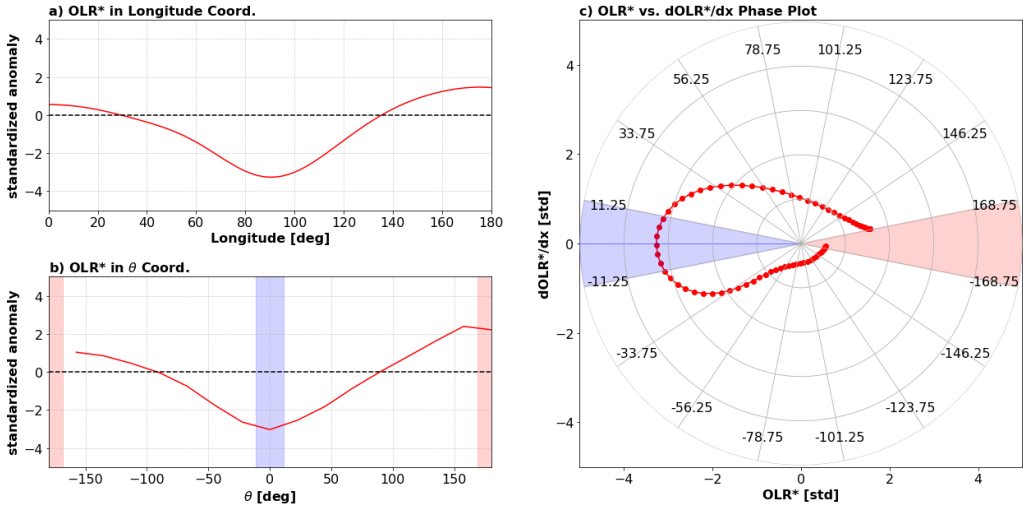

Figure 9: An example of OLR* averaged 5˚ south to north of the latitude centroid for an event within 80–100˚E plotted via (a) standard longitude coordinates and (b) theta coordinates. (c) A zonal phase diagram of the same event defined by OLR* and its zonal gradient. For (c), the data plotted is in longitude coordinates. Red and blue shaded regions in (b) and (c) represent the regions of suppressed convection and active convection, respectively.

Figure 9a-c illustrates this transformation using a MJO event, where Fig. 9a represents the OLR* of the event in longitude coordinates that is averaged from 5° south to north of its latitude centroid. Fig. 9c depicts how this particular event appears on a phase diagram defined by OLR* and its zonal gradient. We divide the zonal phase angle into 16 bins (22.5˚ for each bin) within ±180°. We choose this number to retain enough detail in the resulting plots, while also minimizing the number of theta bins that are unfilled due to the horizontal resolution of the original OLR* data. Variables at longitudes that correspond to each theta bin are averaged and area-weighted according to the number of latitude-longitude points to transform data from longitude to theta coordinate. Fig. 9b represents the OLR* of the event (Fig. 9a) in the transformed theta coordinates. The zonal phase angle represents the relative location with respect to the location of the MJO convective center, where –180˚ is the positive OLR* maximum to the west of the convective center, 0˚ is the negative OLR* at the convective center, and +180˚ is the positive OLR* maximum to the east of the convective center. The red and blue shaded regions in Fig. 9 represent the OLR* maxima and minima, respectively, in this transformed theta coordinate system. This normalizes the scale of the OLR* by its own zonal wavelength.

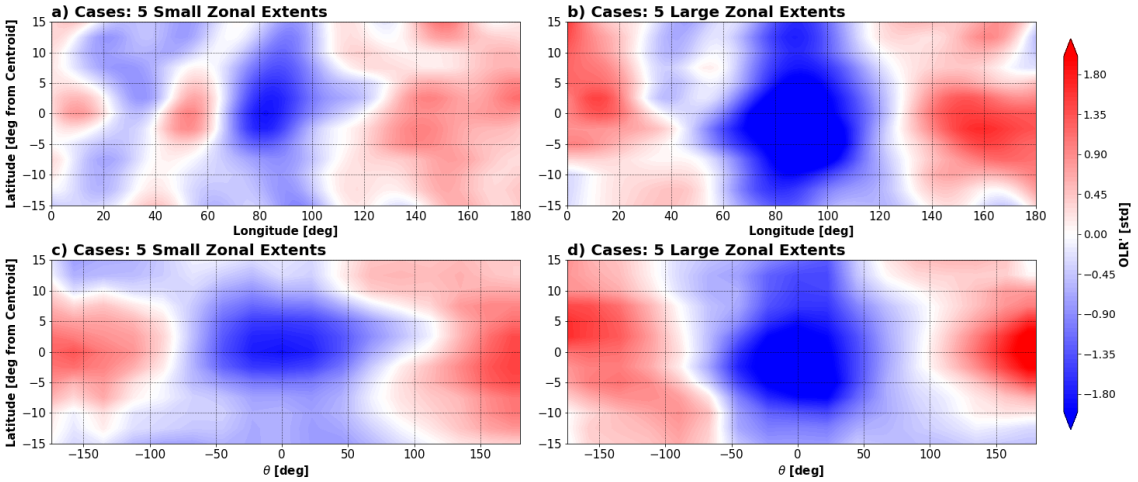

Figure 10: Two-dimensional plots of composite mean OLR* for the (a, c) 5 smallest and (b, d) 5 largest zonal extents of events with maximum OLR* ≤ –2 std. within 80–100˚E. For (a) and (b), data is plotted in longitude-latitude coordinates. For (c) and (d), data is plotted in theta-latitude coordinates. Both show latitudes from 15˚ south to north of the latitude centroid averaged over the duration that the events spend in the longitude range.

An illustration of this effect in two dimensions is shown in Figure 10, where we compare the means of five cases with small zonal extents and five cases with large zonal extents (in longitude coordinates) of stronger negative OLR*. We apply the aforementioned area weighting within each theta bin to conserve the domain-integrated quantities of OLR* (or other variables) between longitude and theta coordinates. As can be seen, the theta coordinate transformation results in an event composite that has comparable zonal scale regardless of its original latitude-longitude composite.

3.2b. Quantification of Rossby-Kelvin circulation signal

We quantify the strength of Kelvin-Rossby circulation using 6-hourly, 2.5° degree zonal wind and geopotential height from ERA-Interim (Dee et al. 2011) data after transforming their longitudes to theta coordinates. The wind and geopotential height are filtered for 20-100 day periods so as to contain only intraseasonal timescale variability. The data are also spatially filtered for zonal wavenumbers 1–10 for both eastward and westward propagation to eliminate noise. We include westward zonal wavenumbers for these variables to include any salient features that may be important to the evolution of the MJO's circulation with longitude, such as westward-propagating Rossby waves associated with the leading convectively suppressed cell present in studies such as D. Kim et al. (2014).

The Rossby-Kelvin signal of MJO events is quantified separately for six 20-degree longitude bins from 40˚E (western Indian Ocean) through 160˚E (western Pacific). The wind and geopotential height anomalies on theta coordinates are averaged among the time steps that the centroid of an MJO event was within each longitude bin. The resultant composite shows the average wind and geopotential structure of each MJO event averaged within the given longitude ranges, normalized by the zonal scale of its convection. Then, to separate the Rossby and Kelvin components of MJO circulation for each event, we must define the regions with respect to the convective center.

Figure 11 shows the composite 850 hPa standardized geopotential height anomalies (Z^*) and anomalous horizontal wind on coordinates defined by theta and latitude relative to convective center for all events when their centroids are within each 20 degree longitude range from 40–60˚E through 140–160˚E. Fig. 11 demonstrates that

the circulation structure of the MJO changes as it moves eastward; therefore, the method of quantifying its circulation should also adjust accordingly.

To identify the locations of anomalous westerlies and easterlies relative to the convective center, we use the standardized zonal wind anomalies in theta coordinates averaged from 5 degrees north to south of the latitude centroid of MJO convection $[U^*(\theta)]$. We further smooth these zonal wind anomalies for each event with a Gaussian filter with a standard deviation of 5° to have a relatively noise-free curve in most cases. Using this smoothed zonal wind composite $[U^*(\theta)]$, we define the region where U^* is 1) greater than or equal to 0.5 (westerly region), 2) less than or equal to -0.5 (easterly region), and 3) between ± 0.5 (neutral region). As we have transformed coordinates from longitude space to θ space in the zonal dimension, the remaining circulation is mapped relative to the convective center at any given time-step. Therefore, based on subsequent composites shown in Figure 11, we define the Kelvin region within the boxes that correspond to the peak in low level easterlies depending on the longitude range being assessed and spanning $\pm 5°$ latitude from the convective center, and then spatially average the quantities within this box to create an index based on the above criteria for U^* for every event within the longitude range. Any labeling of positive, neutral, or negative geopotential anomalies $[Z^*(\theta)]$ within this region is done according to the same method as described above for zonal wind, and indices are created similarly.

3.3. Results

3.3a. Evolution of MJO Circulation Structure

As several previous studies have focused on the MJO when it is centered over the eastern Indian Ocean (e.g. L. Wang et al. 2018, Wang 2019). We first show how the horizontal circulation of the MJO in the low levels evolves as it translates eastward using the composites.

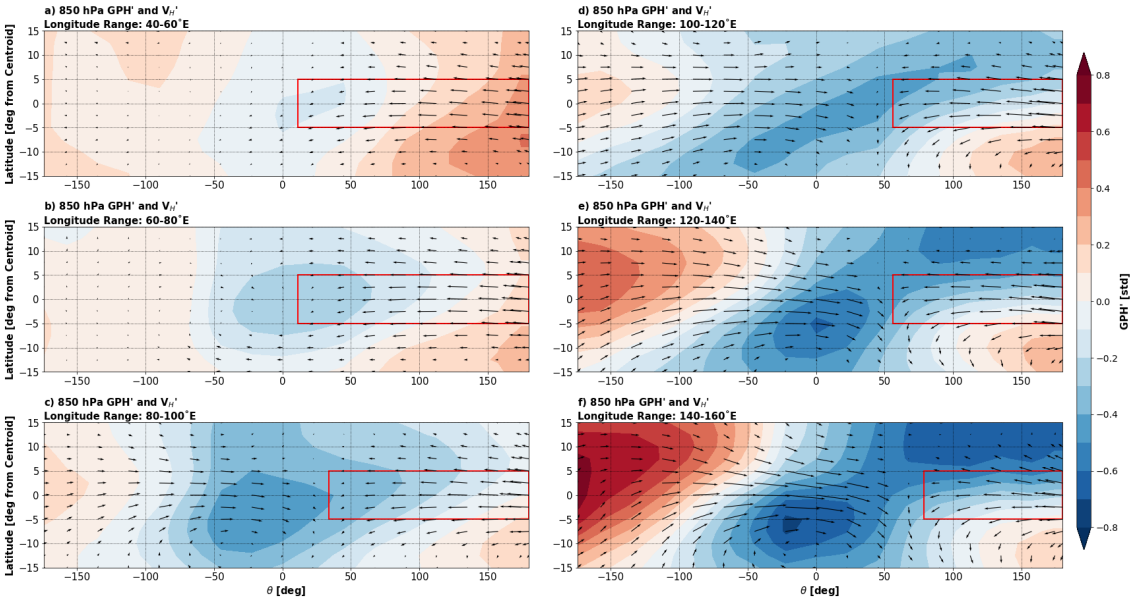

Figure 11: Composite mean 850 hPa Z^* (color-shading, in std) and V_H' (vectors, in m s^{-1}) in theta-latitude coordinates for (a) all cases centered between 40–60˚E, (b) all cases centered between 60–80˚E, (c) all cases centered between 80–100˚E, (d) all cases centered between 100–120˚E, (e) all cases centered between 120–140˚E, and (f) all cases centered between 140–160˚E. Red boxes indicate the regions used to create the zonal wind and geopotential height indices for each longitude range.

When MJO convection is over the Indian Ocean (Fig. 11a–c), the circulation patterns most resemble the theoretical solutions of Matsuno (1966) and Gill (1980). As MJO convection moves eastward, its distinctive negative geopotential height anomaly, with the trailing, flanking Rossby waves and leading Kelvin waves to the east of convective center, all become more well-defined. The wind response within the Rossby region does not become more prevalent until the MJO moves further east, while the Kelvin response is more apparent at all longitudes. Some of this signal is likely attributed to the larger sample size of events and thus greater spread over the Indian Ocean versus regions further east, but the maturation of the convection and circulation further east is in agreement with many previous studies. Similar results are found in Hendon and Salby (1994), and more recently, Adames et al. (2016), specifically the zonal asymmetry of circulation response early in the MJO's lifecycle (see Hsu and Li 2012). Positive height perturbations also appear to the east of the convective center corresponding to the

convectively suppressed region leading the convective center in some cases, which are suggested to play a role in the eastward propagation by D. Kim et al. (2014).

In addition to the change in the amplitude of MJO circulation as it propagates eastward, the Rossby and Kelvin waves begin to shift meridionally northward relative to the latitude of convective center when it reaches 80–100˚E and particularly 100–120˚E. This is consistent with a number of previous studies documenting the shift of MJO convective activity southward relative to the equator during boreal winter as it approaches the Maritime Continent (Wu et al. 2006; Adames et al. 2016; D. Kim et al. 2017). As in Adames et al. (2016), the strongest zonal wind anomalies to the east of the convective center are slightly out of phase meridionally with the peak magnitude in geopotential height anomalies (see their figure 8). The westerly signal in the Rossby region also notably strengthens at these longitudes. Some degree of zonal decoupling of the Rossby and Kelvin waves from each other also occurs over the 100–120˚E range, and continues further eastward. The circulation begins to become decoupled from the convection as the convection begins to de-amplify east of the Indo-Pacific warm pool (Hendon and Salby 1994; Kiladis et al. 2005; Sobel and Kim 2012).

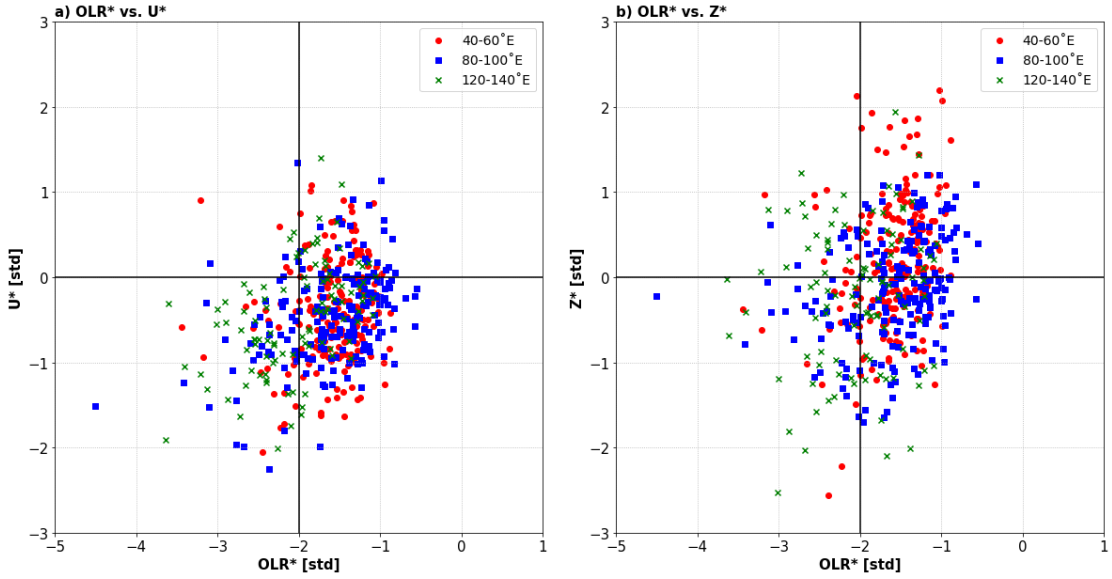

Figure 12: (a) Scatter of the mean OLR* for the 5 theta-latitude grid points containing the strongest negative OLR* values versus U^* east of the convective center for all events in the given reference longitude ranges and (b) as in (a), but for OLR* versus Z^*.

While Fig. 11 shows composites of all MJO events, a large variability in its circulation structure exists among the events. Some MJO events show little signal in the geopotential height field, suggesting either a weak or noisy reflection is present amongst individual events and there also remains a large spread in the patterns of zonal wind anomalies between individual events, with many containing weak easterlies or even westerlies in the Kelvin region (see Figure 12). With many events containing stronger or weaker geopotential height and/or wind anomalies east of the convective center, there is further motivation for the following section, where we statistically assess how the varying circulation characteristics affect propagation.

One may also question potential relationship between the strength of zonal wind or geopotential height anomalies with the amplitude of MJO convection, which could lead to higher probability of continuous eastward propagation. The scatter diagrams shown in Fig. 12 for OLR* versus Z^* and U^* at 40–60, 80–100, and 120–140˚E indicate some linear relationship between the circulation indices and the strength of the MJO convection during the time when the events are present within the reference longitude ranges, namely that stronger negative OLR* is correlated with stronger negative Z^* or U^* in the Kelvin region. However, the r^2 values for these regressions indicate low percentages of variance explained and are not significant at the 95% confidence level, with the exception of U^* at 120–140˚E. Therefore, while some indication of stronger MJO convection leading to a well-developed Kelvin circulation exists, there exists a large amount of variability that warrants further investigation into what is resulting in these changes in circulation strength.

3.3b. Relationship between Kelvin wave signal and MJO Propagation

Previous studies have emphasized the importance of lower tropospheric easterly anomalies to the east of the convective center (e.g. Hsu and Li 2012; Adames and Wallace 2015; Wang et al. 2019). The easterly anomalies associated with the Kelvin wave can moisten the environment east of the MJO through frictional boundary layer moisture convergence, surface fluxes, and horizontal moisture advection, leading to the eastward propagation of the MJO. To assess the importance of the easterlies, Figure 13

shows the probabilities of propagation for MJO events with easterlies east of the convective center, events containing neutral or westerlies east of the convective center, and the difference between the two sets.

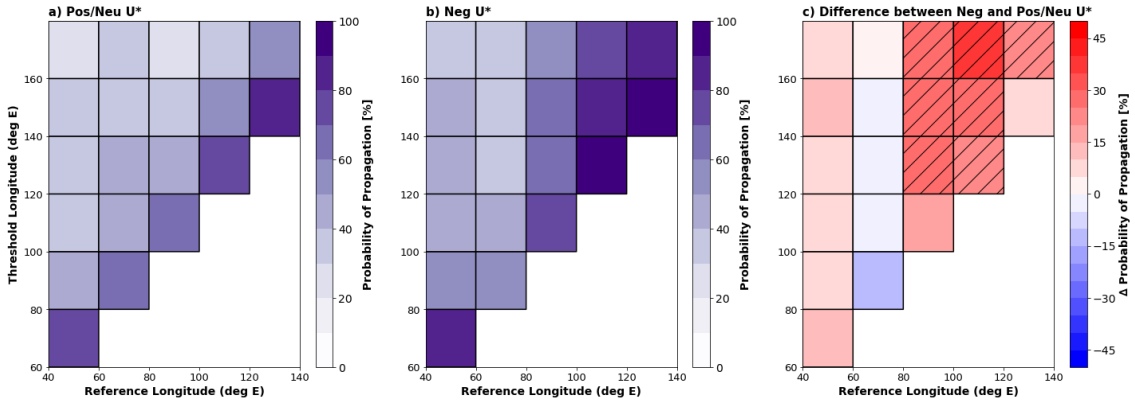

Figure 13: (a) Probabilities of propagation beyond the threshold longitudes given a positive or neutral U^* state east of the convective center at the reference longitude range, (b) as in a), but for negative U^* state, (c) probability difference between the two U^* states. Hatching indicates significance at the 95% confidence level.

The probability of propagation is defined as the percentage of events with a given circulation pattern that propagate beyond the threshold longitude. In other words, if an event contains a particular set of circulation characteristics, such as an easterly Kelvin component in U^*, at 40-60˚E, what is the probability that it propagates downstream beyond 60˚E, 80˚E, 100˚E, and so forth? This is done for each reference longitude range from 40-60˚E through 120–140˚E, which is indicated on the horizontal axes in Fig. 13. Therefore, in Figs. 13a-b, each grid square represents the probability that an event propagates beyond the threshold longitude, given a certain status of zonal wind anomalies east of the convective center at the reference longitude. The vertical axis corresponds to threshold longitudes of propagation. Fig. 13c shows the difference in the likelihood of propagation between those that contain a stronger easterly wind anomaly against a weaker or reversed zonal wind anomaly east of the transition, where positive difference indicates that the events with easterlies have higher probability of propagation. For the reference longitude ranges of 40–60˚E and 60–80˚E, we see relatively small differences in probability of propagation for all threshold longitudes. However, when the convective centers are located between 80–100˚E and 100–120˚E, we see higher odds of propagation for events with stronger easterly wind anomalies,

with statistical significance at the 95% confidence level. These results indicate that, when MJO convection is near or over the Maritime Continent, the presence of easterly wind anomalies to its east enhance the probability of further MJO eastward propagation. While the differences in propagation probabilities at other reference longitudes indicate a higher probability of propagation for events starting out with a stronger easterly anomaly versus weaker (except at 60–80˚E), there is no statistical significance indicated by the Monte-Carlo test. However, statistically significant positive differences were seen when MJO events with easterly anomalies were compared with events with westerlies (i.e., not including neutral cases). These results indicate that MJO events containing a stronger easterly wind anomaly east of the convective center generally propagate further than the events with weaker easterly or westerly winds. This is consistent with the results of Wang et al. (2019), which found that events that successfully propagated through the Maritime Continent contained stronger easterly wind anomalies ahead of the convective center.

While most of the previous works attempting to link the dynamical properties of the MJO with its propagation have focused on wind anomalies due to their physical impacts on the moisture field through convergence and advection (e.g. Hsu and Li 2012; L. Wang et al. 2018; Wang et al. 2019), the dynamics-oriented diagnostics presented in the model comparison study of Wang et al. (2018) provide motivation to look at other aspects of the circulation pattern. In addition, the theoretical Matsuno-Gill solutions define the Kelvin wave as containing a negative pressure perturbation as part of the response, which also encourages boundary layer convergence (Fig. 8). We see this reflected in the composites of Z^* and horizontal wind in Fig. 11. For these reasons, we also assess the statistical relationship between Z^* east of the convective center with probabilities of propagation. Presumably, if a MJO event contains a strong negative height perturbation to the east of the convective center early in its lifecycle, it can mean that the circulation itself is more vigorous. The probabilities of propagation are shown for Z^* east of the convective center in Figure 14.

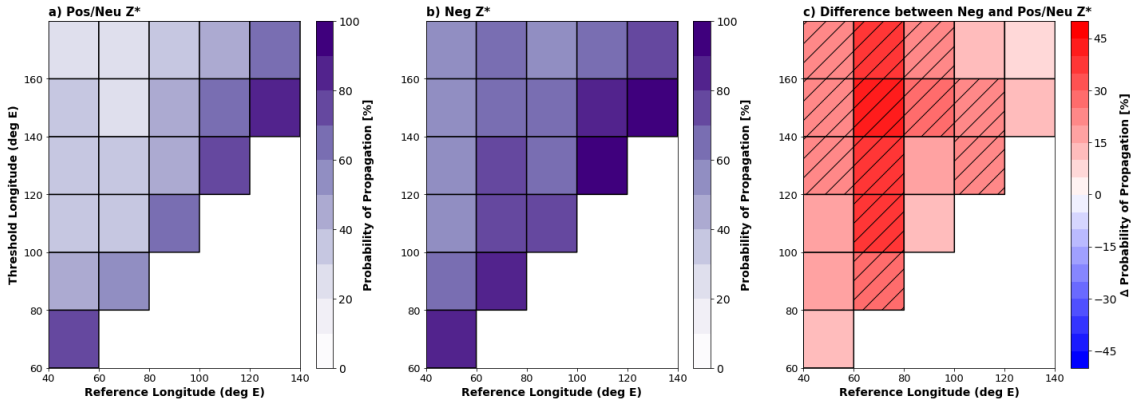

Figure 14: As in Fig. 13, but instead for Z^* states east of the transition.

Unlike those for U^*, there is an immediate statistical relationship with Z^* in the 40–60˚E and especially the 60–80˚E range. Robust positive differences in probability of propagation are present for every threshold longitude from 80˚E through 160˚E, with significance indicated for all grid cells. The differences are particularly strong for the 60–80˚E reference range (i.e., greater than +50% beyond 100˚E longitude). In contrast to the effects of zonal wind anomalies shown in Fig. 13, statistical significance on the impacts of geopotential height anomalies weaken at reference longitudes eastward of 100˚E. Figs. 13 and 14 together indicate that the status of Z^* east of the convective center is more statistically important early in the MJO's lifecycle and the status of U^* is more important once it approaches or enters the Maritime Continent in determining whether the MJO continues to propagate eastward.

The existence of negative geopotential height or easterlies alone does not strictly indicate the presence of Kelvin wave, while the combination of both is a clear indication of the presence of Kelvin wave. Therefore, we test combinations of the two circulation indices east of the transition on MJO propagation probabilities. Figure 15 shows the difference between negative and positive or neutral Z^* given the presence of easterlies.

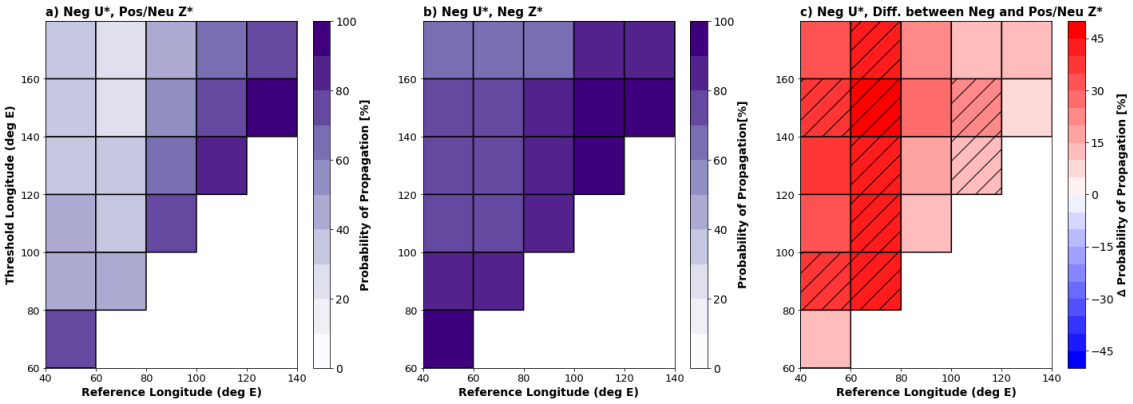

Figure 15: As in Figs. 13 and 14, but instead for cases with negative U^* and differing Z^* states east of the transition.

We analyze these particular combinations as to see what additional information can be gathered from Z^* if we know that the U^* response is already similar to a Kelvin wave. The highest raw probabilities of propagation exist when the MJO event in question contains both negative Z^* and easterlies east of the transition, with values in excess of 70% through most of the grid cells (Fig. 15b). Probability differences given the existence of easterlies are positive between negative Z^* and positive/neutral Z^*, although significance is very similar to the test for Z^* only. The largest positive differences and most consistent significance are for the 40–60˚E and 60–80˚E reference range. This result indicates that the existence of Kelvin wave circulation east of MJO convection that is indicated by the presence of both easterlies and negative geopotential height anomalies lead to the highest propagation probability of the MJO.

To strengthen some of these findings, time–longitude (Hovmoller) diagrams of composite differences in OLR* between those events that contain negative versus positive/neutral Z^* at 60–80˚E reference longitude and U^* at 100–120˚E reference longitude (respectively) are shown in Figures 16 and 17. For an individual MJO event, the y-axis represents the time lag in relation to the middle time-step that the event spent in the reference longitude bin. For the reference longitude ranges of 60–80˚E, the higher probabilities of propagation for negative Z^* (Fig. 14) are corroborated by a significantly stronger and larger in zonal extent OLR* anomaly in these cases propagating downstream to roughly 125˚ longitude before its propagation characteristics begin to change.

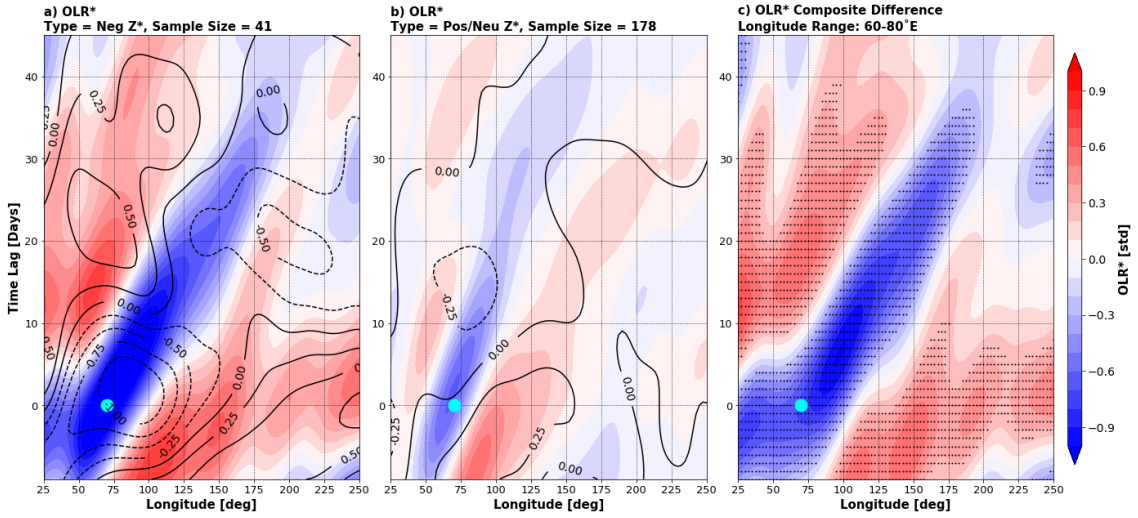

Figure 16: Hovmoller diagrams of (a) OLR* (color shading, in std) and Z^* (contours, in std) for negative Z^* cases east of the convective center at 60–80˚E, (b) as in a), but for positive or neutral Z^* cases, and (c) composite difference between the two Z^* states. Contours are in intervals of 0.25 std. Cyan marker represents the intersection of time lag = 0 and the middle of the reference longitude range. Stipple in c) is indication of significance at the 95% confidence level.

Results are significant at the 95% confidence level until roughly 35 days following the reference time (the middle time that the MJO event spends in the reference longitude range). In contrast, the negative OLR* between the events with easterlies and westerlies, at these two reference longitude ranges (not shown), is both much weaker in amplitude and has a smaller temporal (in the case of 40–60˚E) or spatial (60–80˚E) scale of significance via the Monte-Carlo test.

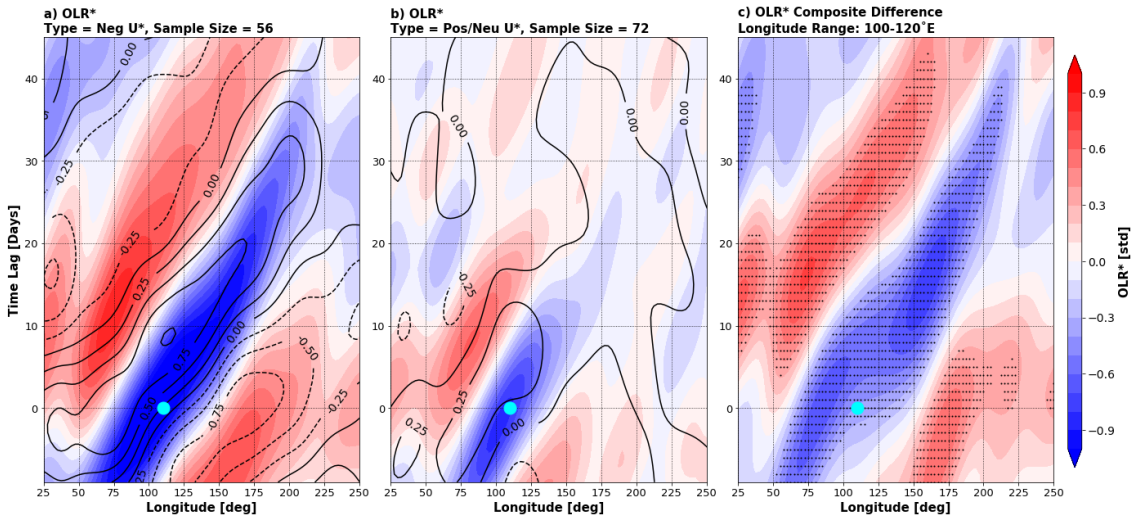

Figure 17: As in Fig. 16, but for U^* states at 100–120˚E. Contours are U^* (std).

We also note in Figs. 16 and 17 that OLR* has a much stronger initial relationship at t = 0 with Z^* than U^*, as indicated by the comparatively weaker differences in the latter and the negative, statistically significant differences in the former. The importance of which circulation index is used again seems to flip somewhat to the east of these longitudes. The region of statistical significance for OLR* between U^* states increases relative in comparison to Z^* in the 80–100˚E, 100–120˚E, and the 120–140˚E longitude ranges. There is very little significance in the differences for OLR* between Z^* states beyond +10–20 days lag in any of these regions (not shown), while U^* consistently shows significance between +35–40 days lag. This adds robustness to the claim that negative Z^* east of the convective center is a stronger statistical indication of further propagation than U^* over the western and central Indian Ocean, with U^* becoming a better indicator further east towards the Maritime Continent.

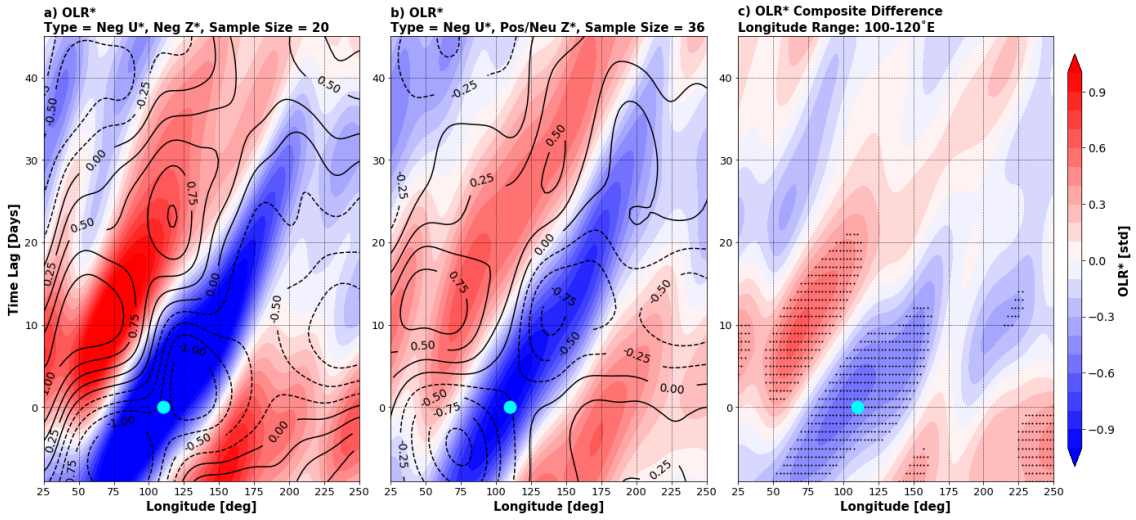

Figure 18: As in Figs. 16 and 17, but for negative U^* with varying Z^* states at 100–120˚E. Contours are Z^* (std).

In Figure 18, we show the difference between negative Z^* and positive or neutral Z^* given negative U^* at the reference longitude range of 100–120˚E. This is one of the longitude ranges where the difference between U^* states individually shows most significance in the probability analysis (Fig. 13). The mean of the negative Z^* cases has a considerably wider region of strong negative OLR*, along with significance through

the first 15 days, showing that even when U^* by itself has the properties of a Kelvin wave downstream of the convective center, it is helpful to also have negative Z^* co-located with it. This result is both consistent with the probability analysis as the MJO propagates through the Maritime Continent towards the West Pacific and is consistent through all of the reference longitude ranges, although weaker significance is indicated for the 120–140˚E and 140–160˚E ranges. Further downstream, the difference becomes negligible between the two sets as the MJO's structure changes in character.

3.4. Summary of Relationship between MJO Circulation and Eastward Propagation

In summary, the analysis presented in this chapter showed that:

I. The method of scaling MJO events by their zonal wavelength in OLR* is effective in its purpose to create more objective compositing between multiple events and in reproducing results shown in previous studies regarding the evolution of the MJO's circulation pattern.

II. The MJO's Rossby/Kelvin circulation pattern tends to decouple slightly upon passage of the Maritime Continent and tends to propagate southward of the equator during NDJFM. The wind response in the Kelvin region develops relatively early in the MJO's evolution, while the wind response in the Rossby region takes longer to develop.

III. The differences in probabilities of propagation between negative and positive/neutral U^* east of the convective center are most robust for MJO events in the 80–100˚E and 100–120˚E reference longitude range. For Z^*, the differences are most robust in the 40–60˚E and 60–80˚E range.

IV. The probabilities of propagation for combinations of U^* and Z^* indices are highest when both U^* and Z^* are in a negative state east of the convective center. In other words, when both criteria for a Kelvin-like circulation response are met.

V. Results of the probability of propagation tests are supported by time-longitude composite differences of OLR* between the relevant U^* and Z^* states east of the convective center.

In the next chapter, we seek to link the statistical results displayed here with physical processes. As the MJO shows coherent evolution with moisture anomalies given the WTG approximation in the tropics (Sobel et al. 2001; Adames and Wallace 2015; Adames and Kim 2016), the Kelvin circulation can influence propagation through its interaction with the moisture field through different processes, which will be diagnosed in the next chapter.

4. The Kelvin Circulation and its Relationship with the Moisture Field

4.1. Background

As suggested in sections 1.2 and 1.3, the role of interactions with moisture in determining the propagation of the MJO is considered vitally important (Kiranmayi and Maloney 2011; Hsu and Li 2012; Sobel and Maloney 2013; D. Kim et al. 2014; Adames and Wallace 2015; Feng et al. 2015; Adames and Kim 2016; Wang and Chen 2017; Wang et al. 2019). Namely, these interactions with the moisture field lead to moistening and destabilization eastward of active convection (Hsu and Li 2012; Sobel and Maloney 2013; DeMott 2018), which spurs cumulus development that eventually grows into more organized convection. Given that the Kelvin circulation exists east of the convection, it follows to that adjusting its characteristics may change the interaction with the moisture field ahead of the convective center. If we increase the strength of the low level easterlies and/or negative geopotential height anomalies within the region to the east of the convective center, is there a corresponding increase in low and/or middle tropospheric moistening downstream that would thereby increase the chances of the MJO continuing to propagate, especially through the longitudes of the Maritime Continent? We will adopt the moisture budget analysis of Adames and Wallace (2015) to accomplish this, and attempt to link the statistical results found in the previous chapter to physical processes.

4.2. Data and Methods

In terms of quantifying the impacts of the circulation on the moisture field, we will use several methods employed in the previous chapter. The respective states of U^* and Z^* east of the convective center will again be used to separate circulation characteristics, and we assess the degree of moisture near the convective center and moistening ahead (east) of convection. Intraseasonal specific humidity anomalies (q') are calculated from ERA-Interim reanalysis through the same filtering method used for the wind and geopotential height anomalies. Three-dimensional moisture budget analysis of the filtered data is performed to assess processes that contribute to moisture

variability associated with MJO events. The corresponding budget terms are calculated following the methods of Yanai et al. (1973) and Adames and Wallace (2015) as

$$\frac{\partial q'}{\partial t} = -\left(u\frac{\partial q}{\partial x}\right)' - \left(v\frac{\partial q}{\partial y}\right)' - \left(\omega\frac{\partial q}{\partial p}\right)' + \frac{Q'_2}{L_v} \qquad \text{(Eq. 4.1)}$$

where q is the specific humidity, u is the zonal wind, v is the meridional wind, ω is the vertical velocity in pressure coordinates, Q_2 is the apparent moisture source or sink (Yanai et al. 1973), and L_v is the latent heat of vaporization. Prime notation indicates MJO-filtered quantities (non-standardized). The left-hand side represents the local time rate of change in specific humidity and the right-hand side terms are as follows from left to right: zonal moisture advection, meridional moisture advection, vertical moisture advection, and the apparent moisture source or sink (Yanai et al. 1973), which represents fluxes generated by unresolved eddies, condensation, and evaporation (Yanai and Johnson 1993). As ERA-Interim contains questionable representation of Q_2 in its treatments as a result of diabatic processes (e.g. Kiranmayi and Maloney 2011), we treat the moisture source or sink as a residual to the remaining terms. Closure of the moisture budget itself does not occur in the reanalysis, which has been documented in studies such as Kiranmayi and Maloney (2011), and may be a result of inadequate precipitation handling (Adames and Wallace 2015) in the reanalysis. We combine the vertical advection and residual terms to yield the net moistening between the two as they nearly cancel each other due to condensation (a moisture sink) from vertical motion. Convective parameterization and linearized large-scale condensation in the reanalysis dominate the contribution to Q_2 (Dee et al. 2011; Adames and Wallace 2015).

Each term in Eq. 4.1 is calculated six hourly and on longitude-latitude domain first before they are composited based on MJO events. All moisture-related quantities on an event-by-event basis are again scaled by the zonal wavelengths of the MJO as described in section 3.2a, in order to provide a perspective relative to the convective center and less dependent on horizontal scale. We use both vertical cross-sections in theta coordinates averaged $\pm 10°$ latitude from the convective center and column-integrated quantities. Column-integrated specific humidity is denoted by $\langle q \rangle =$

$\frac{1}{g}\int_{P_1}^{P_2} q\, dp$ in the subsequent analysis, both to diagnose the altitudes of moistening associated with the MJO and its horizontal structure. All column-integrated quantities and cross-sections are computed from 1000 hPa through 200 hPa unless otherwise specified, which consists of 22 vertical levels. All significance testing, where applicable, is again performed using Monte-Carlo tests at the 95% confidence level.

4.3. Results

4.3a. Circulation and Moisture near the Convective Center

Before assessing the time-evolution of moisture associated with different states of the circulation downstream, it is prudent to question whether or not the moisture near the center of convection changes depending on that circulation or not. It stands to argue that if a moister environment exists near the center of the convection under a given state of zonal wind (U^*) or geopotential height (Z^*) east of the convection, it follows that the downstream moistening of the environment during previous time-steps was more pronounced. As mentioned briefly in Section 4.2, we employ similar methods to Section 3.3b to assess the column-integrated specific humidity anomalies $\langle q' \rangle$ averaged zonally near the convective center of the MJO in the range of $\pm$45° theta and meridionally across $\pm$10° latitude.

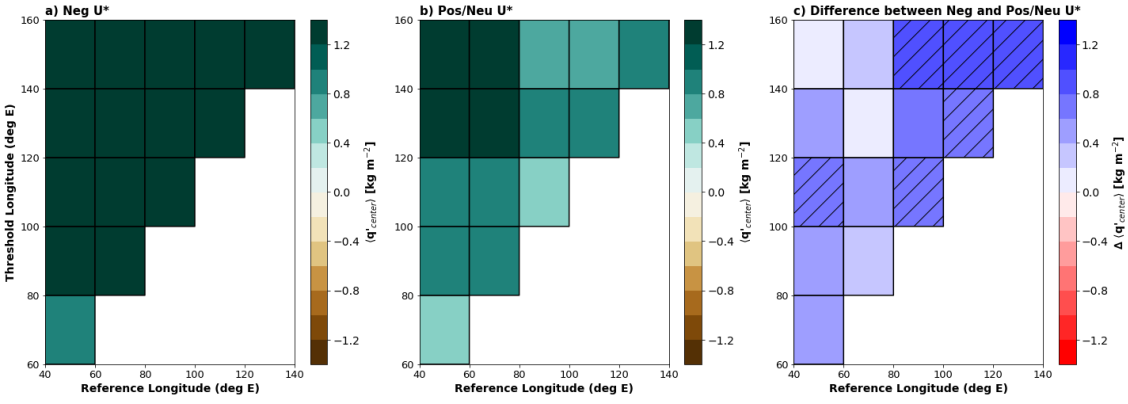

Figure 19: Mean column-integrated q' (kg m^{-2}) averaged between $\pm$45° theta and $\pm$10° latitude from the convective center for cases that start over the given reference longitude ranges with (a) negative U^* and (b) positive or neutral U^* east of the convective center. Panel (c) shows the difference between the two, with diagonal hatching indicating significance at the 95% confidence level.

The results are shown in Figure 19a-b, which depicts the average of $\langle q' \rangle$ within the downstream threshold longitude bins depending on the state of U^* east of the convective center when the MJO is located in the reference longitude bin (at time lag = 0). The difference in $\langle q' \rangle$ between negative U^* and neutral or positive U^* is shown in Fig. 19c, and uniformly shows that positive intraseasonal moisture anomalies near the convective center are larger when U^* is negative within the reference longitude range (see Fig. 12 for relationship with OLR anomalies). Significance at the 95% confidence level is indicated mainly for the reference longitudes from 80°–100°E eastward, which is notable as it generally matches the results found in the probability of propagation analysis (Fig. 13). In other words, a negative state of U^* east of the convective center over the eastern Indian Ocean and Maritime Continent has a statistically higher chance of an event propagating across the Maritime Continent, along with having larger positive intraseasonal moisture anomalies co-located with the convection further east.

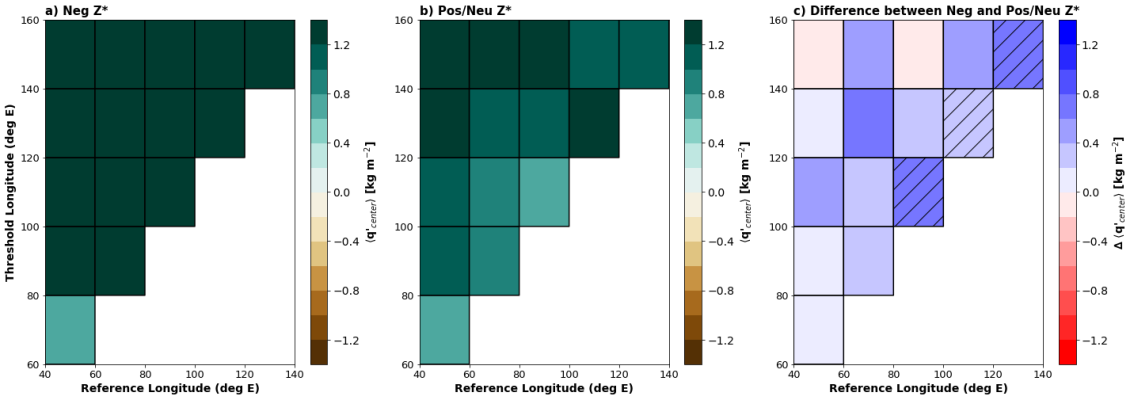

Figure 20: As in Fig. 19, but for Z^* states east of the transition.

Figure 20a-c shows the results in a similar manner for $\langle q' \rangle$ between Z^* states east of the convective center. While Fig. 20c does mostly show positive differences in $\langle q' \rangle$ near the convective center between negative and positive/neutral Z^*, the significance of these results less closely follows the probability of propagation. Namely, the largest positive differences in $\langle q' \rangle$ are more scattered and significance is mainly indicated for the reference longitude ranges of 80–100°E and eastward (and are limited to the longitude bin immediately downstream of the reference longitudes), as opposed to

the probability of propagation analysis where Z^* showed more significance in the western longitude ranges, particularly 60–80˚E (Fig. 14).

4.3b. Relationships between Circulation and Moisture Budget Terms

In order to diagnose the relationship between the circulation indices and moisture budget terms, we compute the mean column-integrated moisture budget terms over the same regions of theta that were used to calculate U^* and Z^*. For simplicity in reading, we hereby refer to the moisture budget terms in Eq. 4.1 from left to right as follows: time tendency as dq/dt, zonal advection as $uadv$, meridional advection as $vadv$, and the combined effects of vertical advection and the residual as $wadv + resid$. To partially account for the meridional shift in the maxima of column-integrated specific humidity time-tendency $\langle dq/dt \rangle$ further east in the propagation of the MJO, we average across $\pm$15° of latitude from the convective center for the moisture budget terms. Figure 21 depicts the linear regression (correlation) coefficients of U^* and Z^* versus all four budget terms above as a function of reference longitude ranges from 40–60˚E through 140–160˚E. In Fig. 21a, a negative correlation coefficient indicates that the moisture budget term tends to have a lower value for MJO events with westerly or neutral wind anomalies ahead of the convective center and a higher value for MJO events with easterly wind anomalies ahead of the convective center.

We see that U^* has a consistent negative correlation (at time lag = 0) across all reference longitude ranges with $\langle dq/dt \rangle$ and the column integrated meridional advection $\langle vadv \rangle$. In other words, a positive time tendency in $\langle q' \rangle$ and a positive contribution to that tendency from $\langle vadv \rangle$ is statistically associated with anomalous, MJO-related, low-level easterly flow east of the convective center. Statistical significance of these correlations is noted for $\langle dq/dt \rangle$ at 40–60˚E and 60–80˚E, while statistical significance is indicated for $\langle vadv \rangle$ at 60–80˚E, 100–120˚E, and 120–140˚E. The sign of U^* correlations with the column-integrated zonal advection $\langle uadv \rangle$ changes from a statistically significantly negative value over 40–60˚E to a statistically significant positive value at 120–140˚E, with values close to zero in between. This result indicates that zonal advection does not generally contribute to the moistening eastward of MJO convection and it is not the key mechanism that supports the eastward

propagation of the MJO. Instead, the existence of easterly wind anomalies supports MJO propagation through meridional advection of moisture, which agrees with some of the findings of D. Kim et al. (2014) and Feng et al. (2015), which both emphasized the role of meridional moisture advection in determining whether an MJO event propagated across the Maritime Continent.

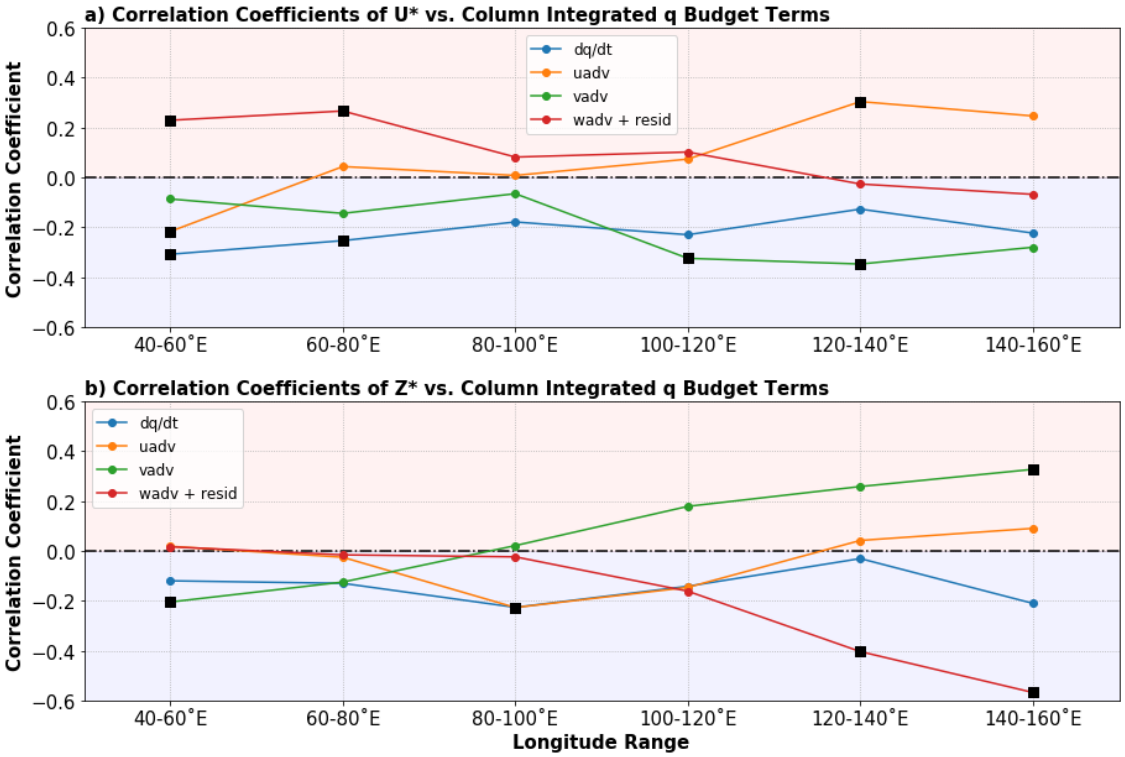

Figure 21: Correlation coefficients of (a) U^* and (b) Z^* east of the convective center versus the column-integrated moisture budget terms (kg m^{-2} day^{-1}) averaged over the same region of theta (according to the longitude range) and over $\pm 15°$ latitude from the convective center. Black square markers indicate statistical significance of the correlations at the 95% confidence level.

Notably, the correlation between U^* with the column-integrated vertical advection and residual term $\langle wadv + resid \rangle$ remains quite small, changes sign more than once, and is insignificant across all of the reference longitude ranges. This result appears to contradict the conclusions by Hsu and Li (2012) and Wang et al. (2019), who suggested that the enhanced low-level Kelvin wave easterlies were associated with enhanced boundary layer moisture convergence (see Fig. 8) and subsequent vertical moistening of the lower troposphere ahead of the convection. A similar analysis as

shown in Fig. 21 was conducted for the low-level integrated moisture budget terms below 700 hPa, and yielded similar results (not shown).

Meanwhile, in Fig. 21b, which depicts the correlations of the column-integrated budget terms with Z^*, the correlation with $\langle dq/dt \rangle$ remains negative across the full range of longitude ranges, but weakens over 120–140˚E, indicating at least a modest inclination for events with negative geopotential height east of the convective center to have more moistening in the same region. There is a flip in the signs of the correlations associated with $\langle vadv \rangle$ and $\langle wadv + resid \rangle$, with correlations near zero around 80–100˚E. The negative correlation with $\langle vadv \rangle$ over the Indian Ocean indicates its contribution to greater moistening when there are negative geopotential height anomalies. However, its correlation sign changes to positive over the Western Pacific, which indicates that the events with negative geopotential height anomalies would tend to have less moistening or drying from $\langle vadv \rangle$ over this region. The reverse is true for $\langle wadv + resid \rangle$. Statistical significance of these correlations is indicated for $\langle vadv \rangle$ at 40–60˚E and $\langle wadv + resid \rangle$ at 120–140˚E and 140–160˚E. Similar results were again found for low-level column integrations of the budget terms (not shown).

The negative correlations of Z^* with $\langle vadv \rangle$ over 40–60˚E and 60–80˚E (whether it be for all cases or only those with easterly U^*) and U^* with $\langle vadv \rangle$ over 80–100˚E, 100–120˚E and 120–140˚E suggest some role of the meridional advection in assisting propagation, as these are the reference longitudes where negative Z^* and easterly U^* have the most significance in the probability of propagation analysis (Figs. 13 and 14). Rather strong, statistically significant negative correlations between Z^* and $\langle wadv + resid \rangle$ east of 100˚E suggests that the boundary layer moisture convergence and associated vertical advection may be related to regions of low pressure within the Kelvin circulation over the Maritime Continent and eastward (Wang and Rui 1990; Wang et al. 2019), but the strength of the low-level easterlies within the Kelvin region alone is not particularly associated with the anomalous vertical moistening of the low-levels (Fig. 21a).

To further assess the vertical structure of the moisture budget terms, Fig. 22 shows their cross-sections averaged over $\pm 10°$ latitude from the convective center over the longitude range of 100–120˚E. Shadings in Fig. 22a-d show the composite

differences of the budget terms between negative and positive/neutral U^* states east of the convective center. Fig. 22a shows statistical significance of the composite difference in local time tendency (dq/dt) and Fig. 22b-d overlays the dq/dt composite difference in contours. Positive differences indicate that there is more moistening contributed by the given budget term for events with easterly U^* and/or negative Z^* versus those that do not. Statistically significant, positive differences in dq/dt primarily exist in the middle troposphere between 700 and 500 hPa, while positive differences in the low-levels are focused further ahead of the convective center roughly from 100° theta eastward. The positive contribution to this low-level tendency between states of U^* is strongly associated with the meridional component ($vadv$), while the sum of the vertical component and residual ($wadv + resid$) and $vadv$ contribute to most of the middle-level tendency difference (consistent with Fig. 21). Again, the importance of the meridional component of moisture advection is suggested over the Maritime Continent (D. Kim et al. 2014; Feng et al. 2015), and having a stronger anomalous, low-level easterly ahead of the convective center favors a larger positive $vadv$ in both the lower and middle troposphere. This pattern consistently appeared across the all of the longitude ranges.

The composite differences between states of Z^* were calculated for the reference longitude range of 60–80˚E for consistency with Ch. 3 (not shown). There are statistically significant positive differences in dq/dt primarily in the middle and upper troposphere ahead of the convective center, and statistically significant negative differences in the lower and middle troposphere immediately behind the convective center. The difference in tendency ahead of the convective center is again primarily related to the horizontal components of moisture advection, particularly $vadv$, except near 500 hPa and above, where a positive difference in $wadv + resid$ exists. The horizontal components also contribute strongly to the negative difference in dq/dt behind the convection.

As in Fig. 21, the results of Fig. 22 suggest the importance of $vadv$ between negative and positive/neutral states of U^* and Z^* over the respective regions where they have the strongest statistical relationships with the probability of propagating downstream.

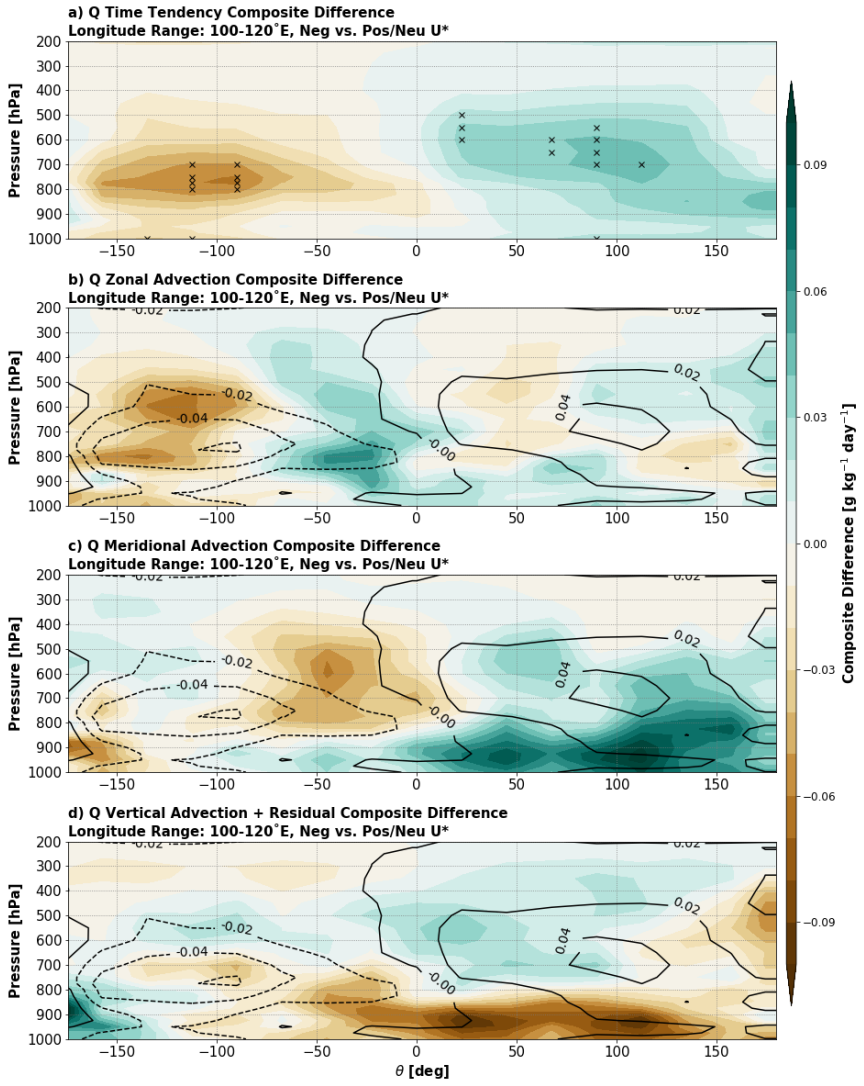

Figure 22: Theta-height cross-section composite differences for events centered at 100–120˚E between negative and positive/neutral U^* of intraseasonal moisture budget terms (color-shaded, in g kg^{-1} day^{-1}) averaged over $\pm$10° latitude from the convective center. For plots (b)-(d), the composite difference of dq/dt is plotted (black contours) and significance at the 95% confidence level (X-stippling) is shown in plot (a) for dq/dt.

In Chapter 3, we showed that the probability of MJO propagation across the Maritime Continent is further enhanced when U^* and Z^* are negative east of the convection. Figure 23 shows the cross-sections for moisture budget terms for MJO events at 100–120˚E, comparing those cases with negative U^* and varying Z^*. We note

that the difference in dq/dt in the low levels is quite small, which is a result primarily of the difference in $vadv$ counter-acting the effects of $wadv + resid$.

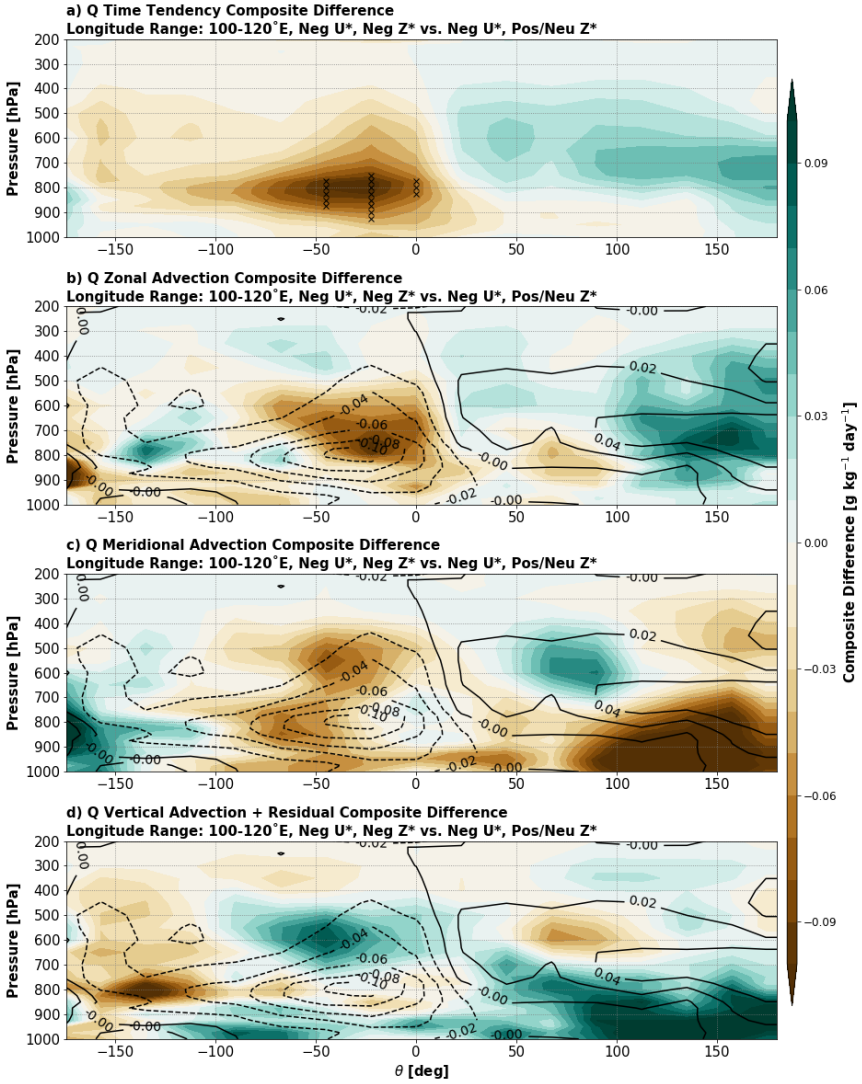

Figure 23: As in Fig. 22, but for negative U^* and negative versus positive/neutral Z^* east of the convective center at 100–120˚E.

In this comparison, the positive (albeit not statistically significant) difference in dq/dt in the middle troposphere is primarily the result of $uadv$, which implies that the zonal advection may have some role in enhancing the propagation probabilities. However, assessing this particular comparison with other longitude ranges surrounding 100–120˚E (not shown), the result is inconsistent as to which component of the moisture advection is most important. The negation of positive contributions in difference by $wadv + resid$ and negative contributions from $vadv$ continues to hold.

Meanwhile, further west in the Indian Ocean, where the largest differences in propagation probabilities (Fig. 15) exist, positive differences in dq/dt are again primarily a result of $vadv$. It is clear from these three comparisons that the adjustments in circulation structure and potentially meridional propagation (Adames et al. 2016; D. Kim et al. 2017) are non-negligible when considering the relationship between MJO-related moisture budget terms and circulation.

In studies such as D. Kim et al. (2014) and Feng et al. (2015) that studied the dichotomy of propagating and non-propagating MJO events across the Maritime Continent, further breakdown of the moisture budget terms into low and high frequency components was conducted. In the former study, which emphasized the role of a strong suppressed convective phase leading the active convection, the advection of free tropospheric (in the layer from 850–200 hPa) mean moisture by anomalous meridional flow associated with anticyclonic Rossby-like circulations generated by the suppressed convective region was key. Feng et al. (2015) found this process occurred during cases with strong-suppressed convection ahead of the convective center and without.

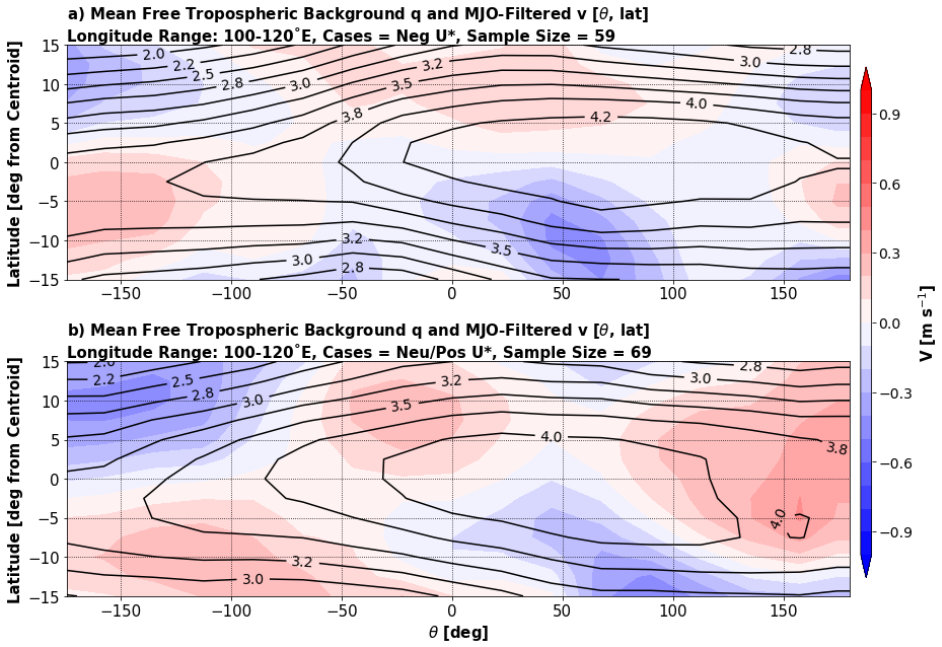

Figure 24: Theta-latitude map of composite mean, column-averaged free tropospheric (850–200 hPa) $\bar{q}$ (contours, in g kg^{-1}) and column-mean, MJO-filtered, free tropospheric meridional wind (color-shaded, in m s^{-1}) for (a) cases with negative and (b) cases with positive/neutral U^* leading the convective center at 100–120˚E.

Figure 24 shows the composite background mean (monthly averaged), free tropospheric specific humidity ($\bar{q}$) and MJO-related meridional wind anomalies (v') between easterly (Fig. 24a) and westerly/neutral (Fig. 24b) U^* events located over 100–120˚E. A comparison between the two panels shows that for the region on either side of the convective center meridionally and bounded by 25–100° theta, there is modestly stronger poleward v' super-positioned with the meridional gradient of $\bar{q}$. Such a configuration would lead to poleward moistening of the free troposphere across this gradient away from the maximum in $\bar{q}$, which may encourage further convective development downstream as it enlarges the region of destabilization ahead of the active convection. The meridional gradient in $\bar{q}$ itself is slightly stronger in the easterly U^* cases, but the positioning, and, to a lesser extent, the strength of the poleward wind anomalies are the more notable differences between the two sets of cases. Similar results were found in a comparison between negative and positive/neutral Z^* cases at 60–80˚E.

In other words, the statistical relationships between the propagation and circulation indices presented in the previous chapter may be partly a result of this difference in free tropospheric moisture advection by the meridional wind component of the MJO. While D. Kim et al. (2014) primarily attributed these features to suppressed convection leading the active convection, Feng et al. (2015) hypothesized that both the suppressed convection and anticyclonic shear of the anomalous easterlies associated with the Kelvin circulation leading the convective center played a role in the development of meridional wind perturbations leading the convective center in propagating cases.

Finally, Figure 25 shows the composite mean MJO-filtered vertical velocity (ω') and background q for events containing negative U^* and Z^* (Fig. 25a) along with negative U^* and positive/neutral Z^* (Fig. 25b) at 100–120˚E. The vertical gradient of background q does not change much between the two states of circulation, but there are larger negative values of ω' (stronger upward motion) for cases where negative Z^* also exists east of the convective center. Given that the highest probabilities for propagation exist across all reference longitude ranges when both circulation indices are negative leading the convective center, this suggests that vertical advection by the MJO-filtered wind of background specific humidity may play a role in aiding propagation.

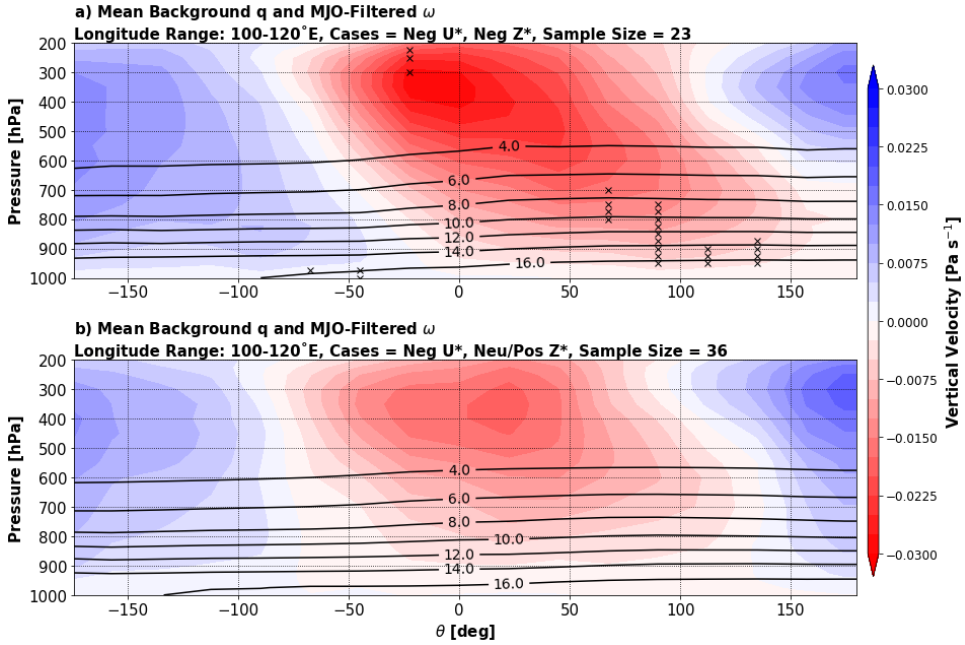

Figure 25: Theta-height cross-section of composite mean background q (contours, in g kg^{-1}) and MJO-filtered vertical velocity (color-shaded, in Pa s^{-1}) for (a) cases with negative U^* and negative Z^* and (b) negative U^* and positive or neutral Z^* leading the convective center at 100–120˚E. X-stippling in (a) indicates significance at the 95% level for vertical velocity.

However, it must be emphasized from Fig. 23c-d that the effects of meridional advection in the low levels at this longitude range tend to counteract those of the combined vertical advection and residual terms, when assessing the composite difference. The largest positive difference in dq/dt in this comparison remains in the mid levels ahead of the convective center, and is primarily contributed by the horizontal advection terms $uadv$ and $vadv$. Fig. 15, which shows the probabilities of propagation for the combined circulation comparison, suggests that the largest differences in probability exist at 40–60˚E and 60–80˚E. Subsequent plots for this comparison computed for these reference longitude ranges (not shown) verify that the meridional component is the largest contributor to positive differences in moistening in the lower and middle troposphere ahead of the convection. In addition, there are similar findings to Fig. 24 suggesting that the advection of mean specific humidity by the meridional wind of the MJO plays a role in encouraging eastward propagation. The primary motivation for Figs. 23 and 25 was to show what additional information could be

gathered from varying Z^* when easterly U^* already had significant relationship with propagation probabilities (e.g. over 100–120˚E).

4.4. Summary of the Relationship between MJO Circulation and Moisture

To summarize the results of this chapter:

I. Both negative geopotential height and easterly zonal wind states east of the convective center are associated with larger positive columnar specific humidity anomalies near the convective center.

II. Correlations of moisture budget terms with Z^* over the Indian Ocean and U^* near/over the Maritime Continent suggest that intraseasonal meridional moisture advection role in moistening ahead of the convective center, particularly through the meridional advection of moisture.

III. Theta-height cross-section composite differences arrive at a similar conclusion that differences in U^* or Z^* may play a role in adjusting the time tendency of moisture ahead of the convective center and associated moisture budget terms, particularly the meridional component.

IV. Differences in the meridional advection of background specific humidity in the free troposphere by MJO-related wind anomalies appear to contribute to the differences in meridional advection, which may be a result of suppressed convection leading the convective center or shear associated with the easterlies within the Kelvin region leading the convective center.

V. In comparisons of the events with easterly U^* and varying Z^* east of the convection over 100–120˚E, the difference in meridional advection negates positive contributions by vertical advection and the residual in the lower troposphere, while zonal advection contributes moistening in the middle

troposphere in negative Z^* cases. At 40–60˚E and 60–80˚E for the same comparison, the meridional component contributes the most to lower-middle tropospheric moistening.

It is worthwhile to mention that this moisture budget analysis is incomplete compared to the analyses of such studies as Kiranmayi and Maloney (2011), D. Kim et al. (2014), and Feng et al. (2015). A more detailed breakdown of the moisture budget terms into their high and low frequency components, in addition to more stringent separation between U^* or Z^* (or the combination of the two) states is warranted to further link the findings in this chapter with those in Ch. 3.

5. Discussions and Conclusion

5.1. Review of Motivations and Methods

The eastward propagation of the MJO, especially over the Maritime Continent, remains an issue in operational and climate models. Over the course of this study, a variety of methods were employed to assess the influence of the circulation response to the convection of the MJO on the propagation of the MJO. More specifically, they were conducted to provide insight into three questions:

1) How does the zonally asymmetric structure of the MJO change as the convective envelope propagates?

2) Does MJO circulation structure have significant consequences on whether the MJO propagates across the Maritime Continent?

3) Through which mechanism does MJO circulation support the eastward propagation of its convection across the Maritime Continent?

We used a new two-dimensional tracking mechanism to follow individual, MJO-filtered OLR anomalies during the NDJFM period from 1979–2018 and limited the cases to those that passed through or initiated over the Indian Ocean. This tracking mechanism compared favorably to one previously employed by Kerns and Chen (2016), which used precipitation. It allows us to follow both zonal and meridional propagation of individual MJO events, as opposed to empirical orthogonal function methods (e.g. Kiladis et al. 2014) or techniques involving Hovmollers (e.g. Feng et al. 2015, Wang et al. 2019). A method of scaling each individual event by the zonal wavelength of the convection was used to yield a perspective relative to the convective center and independent of the zonal scale, which allows us to quantify the circulation response more objectively on a case-by-case basis over differing regions (where circulation

characteristics may change based on Fig. 11). Probability analysis was conducted to test the impact of both the anomalous zonal wind U^* and anomalous geopotential height Z^* within the Kelvin circulation leading the convective center on propagation. Intraseasonal moisture budget analysis was conducted to attempt to link the results found in the probability analysis with physical processes known to affect the evolution of the MJO in the theoretical WTG moisture-mode framework (Sobel et al. 2001; Sobel and Maloney 2012; Adames and Kim 2016) and the trio-interaction framework (Wang and Chen 2017; Chen and Wang 2019).

5.2. Review of Results

Results suggest that eastward propagation extent of the MJO is not significantly affected by the states of QBO and ENSO, although different methods of tracking the MJO or defining QBO or ENSO may affect the results. Our study agrees with Yoo and Son (2016), which found that amplitude of the MJO during boreal winter tends to be higher during easterly QBO. It would be interesting to assess the impacts of different types of ENSO (e.g. central Pacific, basin-wide, or east-based events; Capotondi et al. 2015) on MJO propagation and their corresponding changes in sea surface temperature anomalies and surface fluxes.

The circulation of the MJO changes as it propagates eastward as has been documented in numerous previous studies (e.g. Hendon and Salby 1994; Kiladis et al. 2005). Key features in the composite means at different longitude ranges between 40–60˚E and 140–160˚E (Fig. 11) are the intensification of the Kelvin response east of the convective center and the flanking Rossby responses west of the convective center, along with the southward shift of the convection relative to the circulation over the Maritime Continent longitudes (D. Kim et al. 2017). The first two results are both due to maturation in the circulation and sample size decreasing with eastward extent.

There are statistical links between the circulation east of the convective center and eastward propagation, which change depending on the region assessed. The strongest statistical relationships between U^* east of the convective center and the probability of propagation eastward beyond threshold longitudes exists over the eastern Indian Ocean and Maritime Continent (Fig. 13), while the strongest statistical

relationships between Z^* and the probability of propagation downstream exist over the Indian Ocean, especially around 60–80˚E (Fig. 14). The highest probabilities of propagation for all reference longitudes exist when both U^* and Z^* are negative ahead of the convective center (Fig. 15), suggesting a role of the Kelvin wave response leading the convective center in determining propagation extent.

It was found that the meridional component to the intraseasonal moisture advection had the strongest negative correlation with U^* leading the convective center over the Maritime Continent (Fig. 21a), which may be attributed to enhancement from anticyclonic Rossby-like circulations associated with a suppressed convective phase leading the active convection (D. Kim et al. 2014), anticyclonic shear associated with the anomalous easterlies within the Kelvin wave response, or other features such as high-frequency disturbances (Feng et al. 2015). Circulation response to the east of MJO convection is more complicated than a strictly zonal easterly and does contain a notable meridional component (L. Wang et al. 2018).

Meanwhile, the state of U^* ahead of the convective center does not have a strong correlation with the sum of the vertical advection and residual. This suggests that previous studies such as Wang et al. (2019) that linked further propagation to boundary layer moisture convergence and subsequent vertical moistening of the lower troposphere based on a "stronger Kelvin response" may require consideration of the residual moisture budget terms or at least more in-depth analysis with a larger sample of MJO events. Negative correlations between Z^* and meridional advection east of the convective center exist over the Indian Ocean (Fig. 21b), while negative correlations between Z^* and the sum of vertical advection and the residual exist further eastward.

However, over the regions where Z^*, U^*, or a combination of the two is most important when related with propagation probabilities (Figs. 13–15), the meridional component of moisture advection contributes the largest positive difference in moistening in the lower and middle troposphere east of the convection. Ultimately, the results of Ch. 4 suggest that the relationship between the circulation components leading the convective center and moisture budget terms is complex and the processes driving MJO propagation involving moisture are multi-faceted. It depends both on the circulation indices used and the region where the relationship is examined.

Nevertheless, the importance of the meridional component of moisture advection in the lower and middle troposphere is emphasized when assessing the circulation's impacts on the moisture field.

5.3. Caveats and Recommendations for Future Work

As the features leading the convective center were emphasized in this study, it also makes sense to test the impacts of the flanking Rossby waves trailing the convective center in future work, which was not included in this study. Studies such as Wang and Lee (2017) and L. Wang et al. (2018) used metrics that incorporated the strengths of both the Rossby and Kelvin components to the circulation and found that the fidelity of simulating both components was beneficial to MJO forecasting skill. We suggest that the meridional component of moisture advection east of the convection be more closely examined in future studies, similar to the recommendations of D. Kim et al. (2014) and Feng et al. (2015), in addition to a more detailed breakdown of moisture budget terms into their high-frequency and low-frequency components. In other words, some of the work of previous studies involving moisture or MSE budgeting should be conducted using two-dimensional tracking methods such as the one used in this study and the precipitation-based method of Kerns and Chen (2016) to identify MJO events. The lack of closure in the moisture budget in ERA-Interim (Kiranmayi and Maloney 2011; Adames and Wallace 2015) also presents a caveat to the analysis, as does the derived nature of the vertical velocity fields, although vertical velocity has been shown to be well represented in ERA-Interim compared to satellite observations (Tian et al. 2010; Adames and Wallace 2014b).

The two-dimensional OLR tracking mechanism affords the ability to assess both zonal and meridional propagation of the MJO, it is worthwhile in future work to examine cases that detour south of the Maritime Continent and those that do not (D. Kim et al. 2017) to look for changes in both the circulation patterns and moisture budget terms. We also used criteria (described in section 3.2b) to define states of the circulation that could be adjusted in a number of ways that may affect the results. For example, the definitions of "easterly" or "negative" anomalies and the regions where they are averaged could be changed.

The circulation indices outlined here cannot be directly implemented operationally given the filtering performed in order to yield them, but that does not mean ways of measuring the geopotential height and zonal wind signal associated with the MJO do not exist. We also recommend that tests involving zonal wind and geopotential height indices at different tropospheric levels be conducted, as this study only used indices calculated at 850 hPa. Orographic effects on these circulation components over the Maritime Continent should be considered, along with the diurnal cycle of convection (Zhang and Ling 2017). The role of suppressed convective phases leading the active convection (D. Kim et al. 2014) should be more closely scrutinized, as our OLR tracking mechanism allows analysis of these regions, unlike the tracking mechanism of Kerns and Chen (2016). Analyses with newer and more complete reanalysis datasets such as the ERA5 reanalysis (Hersbach et al. 2020) should be conducted to expand the sample size of MJO events, in addition to the use of convection-permitting models on the smaller scale.

The addition of geopotential height as a circulation index for the MJO may provide more information, per the results of this study. Since the results from Ch. 3 indicate some importance of the circulation structure east of the convective center in determining propagation, it would be interesting to assess whether statistical models could implement some of this information into forecasting whether an MJO event will propagate across the Maritime Continent. Such tests would compare the skill of these statistical models in forecasting the eastward extent of propagation given certain states of the low-level zonal wind and geopotential height. Development of further diagnostic indices using both observations and modelling in order to measure the circulation of the MJO is encouraged to test fidelity in simulating propagation of the MJO (e.g. Wang et al. 2018), especially across the Maritime Continent.

References

Adames, Á. F., and D. Kim, 2016: The MJO as a dispersive, convectively coupled moisture wave: Theory and observations. *J. Atmos. Sci.*, https://doi.org/10.1175/JAS-D-15-0170.1.

Adames, Á. F., and J. M. Wallace, 2014a: Three-dimensional structure and evolution of the vertical velocity and divergence fields in the MJO. *J. Atmos. Sci.*, https://doi.org/10.1175/JAS-D-14-0091.1.

Adames, Á. F., and J. M. Wallace, 2014b: Three-dimensional structure and evolution of the MJO and its relation to the mean flow. *J. Atmos. Sci.*, https://doi.org/10.1175/JAS-D-13-0254.1.

Adames, Á. F., and J. M. Wallace, 2015: Three-dimensional structure and evolution of the moisture field in the MJO. *J. Atmos. Sci.*, https://doi.org/10.1175/JAS-D-15-0003.1.

Adames, F. Á., J. M. Wallace, and J. M. Monteiro, 2016: Seasonality of the structure and propagation characteristics of the MJO. *J. Atmos. Sci.*, https://doi.org/10.1175/JAS-D-15-0232.1.

Ahn, M. S., D. Kim, Y. G. Ham, and S. Park, 2020: Role of maritime continent land convection on the mean state and MJO propagation. *J. Clim.*, https://doi.org/10.1175/JCLI-D-19-0342.1.

Barrett, B. S., and L. M. Leslie, 2009: Links between tropical cyclone activity and Madden-Julian oscillation phase in the North Atlantic and Northeast Pacific basins. *Mon. Weather Rev.*, https://doi.org/10.1175/2008MWR2602.1.

Benedict, J. J., and D. A. Randall, 2007: Observed characteristics of the MJO relative to maximum rainfall. *J. Atmos. Sci.*, https://doi.org/10.1175/JAS3968.1.

Bessafi, M., and M. C. Wheeler, 2006: Modulation of south Indian Ocean tropical cyclones by the Madden-Julian Oscillation and convectively coupled equatorial waves. *Mon. Weather Rev.*, https://doi.org/10.1175/MWR3087.1.

Bin Wang, and Hualan Rui, 1990: Dynamics of the coupled moist Kelvin-Rossby wave on an equatorial β-plane. *J. Atmos. Sci.*, https://doi.org/10.1175/1520-0469(1990)047<0397:dotcmk>2.0.co;2.

Capotondi, A., and Coauthors, 2015: Understanding enso diversity. *Bull. Am. Meteorol. Soc.*, https://doi.org/10.1175/BAMS-D-13-00117.1.

Cassou, C., 2008: Intraseasonal interaction between the Madden-Julian Oscillation and the North Atlantic Oscillation. *Nature*, https://doi.org/10.1038/nature07286.

Chang, C.-P., Z. Wang, and H. Hendon, 2006: The Asian winter monsoon. *The Asian Monsoon*.

Chen, G., and B. Wang, 2020: Circulation Factors Determining the Propagation Speed of the Madden–Julian Oscillation. *J. Clim.*, https://doi.org/10.1175/jcli-d-19-0661.1.

Chen, G., and B. Wang, 2019: Dynamic moisture mode versus moisture mode in MJO dynamics: importance of the wave feedback and boundary layer convergence feedback. *Clim. Dyn.*, https://doi.org/10.1007/s00382-018-4433-7.

Dee, D. P., and Coauthors, 2011: The ERA-Interim reanalysis: Configuration and performance of the data assimilation system. *Q. J. R. Meteorol. Soc.*, https://doi.org/10.1002/qj.828.

DeMott, C. A., B. O. Wolding, E. D. Maloney, and D. A. Randall, 2018: Atmospheric Mechanisms for MJO Decay Over the Maritime Continent. *J. Geophys. Res. Atmos.*, https://doi.org/10.1029/2017JD026979.

Dias, J., N. Sakaeda, G. N. Kiladis, and K. Kikuchi, 2017: Influences of the MJO on the space-time organization of tropical convection. *J. Geophys. Res.*, https://doi.org/10.1002/2017JD026526.

Feng, J., T. Li, and W. Zhu, 2015: Propagating and nonpropagating MJO events over maritime continent. *J. Clim.*, https://doi.org/10.1175/JCLI-D-15-0085.1.

Ferranti, L., T. N. Palmer, F. Molteni, and E. Klinker, 1990: Tropical-extratropical interaction associated with the 30-60 day oscillation and its impact on medium and extended range prediction. *J. Atmos. Sci.*, https://doi.org/10.1175/1520-0469(1990)047<2177:TEIAWT>2.0.CO;2.

Fu, J. X., J. Y. Lee, B. Wang, W. Wang, and F. Vitart, 2013: Intraseasonal forecasting of the Asian summer monsoon in four operational and research models. *J. Clim.*, https://doi.org/10.1175/JCLI-D-12-00252.1.

Gill, A. E., 1980: Some simple solutions for heat-induced tropical circulation. *Q. J. R. Meteorol. Soc.*, https://doi.org/10.1002/qj.49710644905.

Gonzalez, A. O., and X. Jiang, 2017: Winter mean lower tropospheric moisture over the Maritime Continent as a climate model diagnostic metric for the propagation of the Madden-Julian oscillation. *Geophys. Res. Lett.*, https://doi.org/10.1002/2016GL072430.

Gottschalck, J., P. E. Roundy, C. J. Schreck, A. Vintzileos, and C. Zhang, 2013: Large-scale atmospheric and oceanic conditions during the 2011-12 DYNAMO field campaign. *Mon. Weather Rev.*, https://doi.org/10.1175/MWR-D-13-00022.1.

Gutzler, D. S., and R. M. Ponte, 1990: Exchange of momentum among atmosphere, ocean, and solid earth associated with the Madden-Julian oscillation. *J. Geophys. Res.*, https://doi.org/10.1029/jd095id11p18679.

Hall, J. D., A. J. Matthews, and D. J. Karoly, 2001: The modulation of tropical cyclone activity in the Australian region by the Madden-Julian oscillation. *Mon. Weather Rev.*, https://doi.org/10.1175/1520-0493(2001)129<2970:TMOTCA>2.0.CO;2.

Hamill, T. M., and G. N. Kiladis, 2014: Skill of the MJO and Northern Hemisphere blocking in GEFS medium-range reforecasts. *Mon. Weather Rev.*, https://doi.org/10.1175/MWR-D-13-00199.1.

Hayashi, Y., 1982: Space-Time Spectral Analysis and its Applications to Atmospheric Waves. *J. Meteorol. Soc. Japan. Ser. II*, https://doi.org/10.2151/jmsj1965.60.1_156.

Henderson, S. A., E. D. Maloney, and E. A. Barnes, 2016: The influence of the Madden-Julian oscillation on Northern Hemisphere winter blocking. *J. Clim.*, https://doi.org/10.1175/JCLI-D-15-0502.1.

Hendon, H. H., and S. Abhik, 2018: Differences in Vertical Structure of the Madden-Julian Oscillation Associated With the Quasi-Biennial Oscillation. *Geophys. Res. Lett.*, https://doi.org/10.1029/2018GL077207.

Hendon, H. H., and M. L. Salby, 1994: The Life Cycle of the Madden–Julian Oscillation. *J. Atmos. Sci.*, https://doi.org/10.1175/1520-0469(1994)051<2225:tlcotm>2.0.co;2.

Hersbach, H., and Coauthors, 2020: The ERA5 global reanalysis. *Q. J. R. Meteorol. Soc.*, https://doi.org/10.1002/qj.3803.

Higgins, R. W., and W. Shi, 2001: Intercomparison of the principal modes of interannual and intraseasonal variability of the North American Monsoon System. *J. Clim.*, https://doi.org/10.1175/1520-0442(2001)014<0403:IOTPMO>2.0.CO;2.

Hsu, P. C., and T. Li, 2012: Role of the boundary layer moisture asymmetry in causing the eastward propagation of the Madden-Julian oscillation. *J. Clim.*, https://doi.org/10.1175/JCLI-D-11-00310.1.

Huang, B., and Coauthors, 2017: Extended reconstructed Sea surface temperature, Version 5 (ERSSTv5): Upgrades, validations, and intercomparisons. *J. Clim.*, https://doi.org/10.1175/JCLI-D-16-0836.1.

Hung, C. S., and C. H. Sui, 2018: A diagnostic study of the evolution of the MJO from Indian Ocean to Maritime Continent: Wave dynamics versus advective moistening processes. *J. Clim.*, https://doi.org/10.1175/JCLI-D-17-0139.1.

Hung, M. P., J. L. Lin, W. Wang, D. Kim, T. Shinoda, and S. J. Weaver, 2013: Mjo and convectively coupled equatorial waves simulated by CMIP5 climate models. *J. Clim.*, https://doi.org/10.1175/JCLI-D-12-00541.1.

Jiang, X., 2017: Key processes for the eastward propagation of the madden-julian oscillation based on multimodel simulations. *J. Geophys. Res.*, https://doi.org/10.1002/2016JD025955.

Jiang, X., and Coauthors, 2020: Fifty Years of Research on the Madden-Julian Oscillation: Recent Progress, Challenges, and Perspectives. *J. Geophys. Res. Atmos.*, https://doi.org/10.1029/2019JD030911.

Jiang, X., and Coauthors, 2015: Vertical structure and physical processes of the madden-julian oscillation: Exploring key model physics in climate simulations. *J. Geophys. Res.*, https://doi.org/10.1002/2014JD022375.

Johnson, R. H., and P. E. Ciesielski, 2017: Multiscale variability of the atmospheric boundary layer during DYNAMO. *J. Atmos. Sci.*, https://doi.org/10.1175/JAS-D-17-0182.1.

Kemball-Cook, S. R., and B. C. Weare, 2001: The onset of convection in the Madden-Julian oscillation. *J. Clim.*, https://doi.org/10.1175/1520-0442(2001)014<0780:TOOCIT>2.0.CO;2.

Kerns, B. W., and S. S. Chen, 2016: Large-scale precipitation tracking and the MJO over the Maritime Continent and Indo-Pacific warm pool. *J. Geophys. Res.*, https://doi.org/10.1002/2015JD024661.

Kerns, B. W., and S. S. Chen, 2020: A 20-Year Climatology of Madden-Julian Oscillation Convection: Large-Scale Precipitation Tracking From TRMM-GPM Rainfall. *J. Geophys. Res. Atmos.*, https://doi.org/10.1029/2019JD032142.

Kiladis, G. N., J. Dias, K. H. Straub, M. C. Wheeler, S. N. Tulich, K. Kikuchi, K. M. Weickmann, and M. J. Ventrice, 2014: A comparison of OLR and circulation-based indices for tracking the MJO. *Mon. Weather Rev.*, https://doi.org/10.1175/MWR-D-13-00301.1.

Kiladis, G. N., K. H. Straub, and P. T. Haertel, 2005: Zonal and vertical structure of the Madden-Julian oscillation. *J. Atmos. Sci.*, https://doi.org/10.1175/JAS3520.1.

Kim, D., and Coauthors, 2009: Application of MJO simulation diagnostics to climate models. *J. Clim.*, https://doi.org/10.1175/2009JCLI3063.1.

Kim, D., H. Kim, and M. I. Lee, 2017: Why does the MJO detour the Maritime Continent during austral summer? *Geophys. Res. Lett.*, https://doi.org/10.1002/2017GL072643.

Kim, D., J. S. Kug, and A. H. Sobel, 2014: Propagating versus nonpropagating Madden-Julian oscillation events. *J. Clim.*, https://doi.org/10.1175/JCLI-D-13-00084.1.

Kim, H. M., D. Kim, F. Vitart, V. E. Toma, J. S. Kug, and P. J. Webster, 2016: MJO propagation across the maritime continent in the ECMWF ensemble prediction system. *J. Clim.*, https://doi.org/10.1175/JCLI-D-15-0862.1.

Kim, H. M., P. J. Webster, V. E. Toma, and D. Kim, 2014: Predictability and prediction skill of the MJO in two operational forecasting systems. *J. Clim.*, https://doi.org/10.1175/JCLI-D-13-00480.1.

Kim, H., F. Vitart, and D. E. Waliser, 2018: Prediction of the Madden-Julian oscillation: A review. *J. Clim.*, https://doi.org/10.1175/JCLI-D-18-0210.1.

Kim, H., M. I. Lee, D. Kim, H. S. Kang, and Y. K. Hyun, 2018: Representation of boreal winter MJO and its teleconnection in a dynamical ensemble seasonal prediction system. *J. Clim.*, https://doi.org/10.1175/JCLI-D-18-0039.1.

Kiranmayi, L., and E. D. Maloney, 2011: Intraseasonal moist static energy budget in reanalysis data. *J. Geophys. Res. Atmos.*, https://doi.org/10.1029/2011JD016031.

Klotzbach, P. J., 2010: On the Madden-Julian oscillation-atlantic hurricane relationship. *J. Clim.*, https://doi.org/10.1175/2009JCLI2978.1.

L'Heureux, M. L., and R. W. Higgins, 2008: Boreal winter links between the Madden-Julian oscillation and the arctic oscillation. *J. Clim.*, https://doi.org/10.1175/2007JCLI1955.1.

Lawrence, D. M., and P. J. Webster, 2002: The boreal summer intraseasonal oscillation: Relationship between northward and eastward movement of convection. *J. Atmos. Sci.*, https://doi.org/10.1175/1520-0469(2002)059<1593:TBSIOR>2.0.CO;2.

Liebmann, B., H. H. Hendon, and J. D. Glick, 1994: The relationship between tropical cyclones of the western pacific and indian oceans and the Madden-Julian oscillation. *J. Meteorol. Soc. Japan*, https://doi.org/10.2151/jmsj1965.72.3_401.

Liebmann, B., and Smith A, 1996: Outgoing long-wave radiation. *Bull. Am. Meteorol. Soc.*,.

Lim, Y., S. W. Son, and D. Kim, 2018: MJO prediction skill of the subseasonal-to-seasonal prediction models. *J. Clim.*, https://doi.org/10.1175/JCLI-D-17-0545.1.

Lin, H., G. Brunet, and J. Derome, 2009: An observed connection between the North Atlantic oscillation and the Madden-Julian oscillation. *J. Clim.*, https://doi.org/10.1175/2008JCLI2515.1.

Lin, H., G. Brunet, and J. Derome, 2008: Forecast skill of the Madden-Julian oscillation in two canadian atmospheric models. *Mon. Weather Rev.*, https://doi.org/10.1175/2008MWR2459.1.

Ling, J., P. Bauer, P. Bechtold, A. Beljaars, R. Forbes, F. Vitart, M. Ulate, and C. Zhang, 2014: Global versus local MJO forecast skill of the ECMWF model during DYNAMO. *Mon. Weather Rev.*, https://doi.org/10.1175/MWR-D-13-00292.1.

Ling, J., C. Zhang, R. Joyce, P. ping Xie, and G. Chen, 2019: Possible Role of the Diurnal Cycle in Land Convection in the Barrier Effect on the MJO by the Maritime Continent. *Geophys. Res. Lett.*, https://doi.org/10.1029/2019GL081962.

Lo, F., and H. H. Hendon, 2000: Empirical extended-range prediction of the Madden-Julian oscillation. *Mon. Weather Rev.*, https://doi.org/10.1175/1520-0493(2000)128<2528:eerpot>2.0.co;2.

Lorenz, D. J., and D. L. Hartmann, 2006: The effect of the MJO on the North American monsoon. *J. Clim.*, https://doi.org/10.1175/JCLI3684.1.

Madden, R. A., and P. R. Julian, 1994: Observations of the 40-50-day tropical oscillation - a review. *Mon. Weather Rev.*, https://doi.org/10.1175/1520-0493(1994)122<0814:OOTDTO>2.0.CO;2.

Madden, R. A., and P. R. Julian, 1971: Detection of a 40–50 Day Oscillation in the Zonal Wind in the Tropical Pacific. *J. Atmos. Sci.*, https://doi.org/10.1175/1520-0469(1971)028<0702:doadoi>2.0.co;2.

Madden, R. A., and P. R. Julian, 1972: Description of Global-Scale Circulation Cells in the Tropics with a 40–50 Day Period. *J. Atmos. Sci.*, https://doi.org/10.1175/1520-0469(1972)029<1109:dogscc>2.0.co;2.

Maloney, E. D., and D. L. Hartmann, 2001: The Madden-Julian oscillation, barotropic dynamics, and North Pacific tropical cyclone formation. Part I: Observations. *J. Atmos. Sci.*, https://doi.org/10.1175/1520-0469(2001)058<2545:TMJOBD>2.0.CO;2.

Maloney, E. D., and D. L. Hartmann, 2000: Modulation of hurricane activity in the Gulf of Mexico by the Madden- Julian oscillation. *Science (80-.).*, https://doi.org/10.1126/science.287.5460.2002.

Marshall, A. G., H. H. Hendon, S. W. Son, and Y. Lim, 2017: Impact of the quasi-biennial oscillation on predictability of the Madden–Julian oscillation. *Clim. Dyn.*, https://doi.org/10.1007/s00382-016-3392-0.

Martin, Z., S. Wang, J. Nie, and A. Sobel, 2019: The impact of the QBO on MJO convection in cloud-resolving simulations. *J. Atmos. Sci.*, https://doi.org/10.1175/JAS-D-18-0179.1.

Matsuno, T., 1966: Quasi-Geostrophic Motions in the Equatorial Area. *J. Meteorol. Soc. Japan. Ser. II*, https://doi.org/10.2151/jmsj1965.44.1_25.

Moon, J. Y., B. Wang, and K. J. Ha, 2011: ENSO regulation of MJO teleconnection. *Clim. Dyn.*, https://doi.org/10.1007/s00382-010-0902-3.

Nishimoto, E., and S. Yoden, 2017: Influence of the stratospheric quasi-biennial oscillation on the Madden-Julian oscillation during austral summer. *J. Atmos. Sci.*, https://doi.org/10.1175/JAS-D-16-0205.1.

Pai, D. S., J. Bhate, O. P. Sreejith, and H. R. Hatwar, 2011: Impact of MJO on the intraseasonal variation of summer monsoon rainfall over India. *Clim. Dyn.*, https://doi.org/10.1007/s00382-009-0634-4.

Peatman, S. C., A. J. Matthews, and D. P. Stevens, 2014: Propagation of the Madden-Julian Oscillation through the Maritime Continent and scale interaction with the diurnal cycle of precipitation. *Q. J. R. Meteorol. Soc.*, https://doi.org/10.1002/qj.2161.

Pritchard, M. S., and C. S. Bretherton, 2014: Causal evidence that rotational moisture advection is critical to the superparameterized Madden-Julian oscillation. *J. Atmos. Sci.*, https://doi.org/10.1175/JAS-D-13-0119.1.

Raymond, D. J., and Z. Fuchs, 2009: Moisture modes and the Madden-Julian oscillation. *J. Clim.*, https://doi.org/10.1175/2008JCLI2739.1.

Riley, E. M., B. E. Mapes, and S. N. Tulich, 2011: Clouds associated with the Madden-Julian oscillation: A new perspective from Cloudsat. *J. Atmos. Sci.*, https://doi.org/10.1175/JAS-D-11-030.1.

Rowe, A. K., and R. A. Houze, 2015: Cloud organization and growth during the transition from suppressed to active MJO conditions. *J. Geophys. Res.*, https://doi.org/10.1002/2014JD022948.

Sakaeda, N., G. Kiladis, and J. Dias, 2020: The Diurnal Cycle of Rainfall and the Convectively Coupled Equatorial Waves over the Maritime Continent. *J. Clim.*, https://doi.org/10.1175/jcli-d-19-0043.1.

Seo, K. H., W. Wang, J. Gottschalck, Q. Zhang, J. K. E. Schemm, W. R. Higgins, and A. Kumar, 2009: Evaluation of MJO forecast skill from several statistical and dynamical forecast models. *J. Clim.*, https://doi.org/10.1175/2008JCLI2421.1.

Singh, S. V., R. H. Kripalani, and D. R. Sikka, 1992: Interannual variability of the Madden-Julian oscillations in Indian summer monsoon rainfall. *J. Clim.*, https://doi.org/10.1175/1520-0442(1992)005<0973:IVOTMJ>2.0.CO;2.

Sobel, A. H., and D. Kim, 2012: The MJO-Kelvin wave transition. *Geophys. Res. Lett.*, https://doi.org/10.1029/2012GL053380.

Sobel, A. H., J. Nilsson, and L. M. Polvani, 2001: The weak temperature gradient approximation and balanced tropical moisture waves. *J. Atmos. Sci.*, https://doi.org/10.1175/1520-0469(2001)058<3650:TWTGAA>2.0.CO;2.

Sobel, A., and E. Maloney, 2012: An idealized semi-empirical framework for modeling the Madden-Julian oscillation. *J. Atmos. Sci.*, https://doi.org/10.1175/JAS-D-11-0118.1.

Sobel, A., and E. Maloney, 2013: Moisture modes and the eastward propagation of the MJO. *J. Atmos. Sci.*, https://doi.org/10.1175/JAS-D-12-0189.1.

Son, S. W., Y. Lim, C. Yoo, H. H. Hendon, and J. Kim, 2017: Stratospheric control of the madden-julian oscillation. *J. Clim.*, https://doi.org/10.1175/JCLI-D-16-0620.1.

Sperber, K. R., 2003: Propagation and the vertical structure of the Madden-Julian oscillation. *Mon. Weather Rev.*, https://doi.org/10.1175/1520-0493(2003)131<3018:PATVSO>2.0.CO;2.

Straub, K. H., 2013: MJO initiation in the real-time multivariate MJO index. *J. Clim.*, https://doi.org/10.1175/JCLI-D-12-00074.1.

Tian, B., D. E. Waliser, E. J. Fetzer, and Y. L. Yung, 2010: Vertical moist thermodynamic structure of the Madden-Julian oscillation in atmospheric infrared sounder retrievals: An update and a comparison to ECMWF interim Re-Analysis. *Mon. Weather Rev.*, https://doi.org/10.1175/2010MWR3486.1.

Trenberth, K. E., and D. P. Stepaniak, 2001: Indices of El Niño evolution. *J. Clim.*, https://doi.org/10.1175/1520-0442(2001)014<1697:LIOENO>2.0.CO;2.

Virts, K. S., and J. M. Wallace, 2010: Annual, interannual, and intraseasonal variability of tropical tropopause transition layer cirrus. *J. Atmos. Sci.*, https://doi.org/10.1175/2010JAS3413.1.

Vitart, F., and F. Molteni, 2010: Simulation of the Madden-Julian oscillation and its teleconnections in the ECMWF forecast system. *Q. J. R. Meteorol. Soc.*, https://doi.org/10.1002/qj.623.

Waliser, D., and Coauthors, 2006: The experimental MJO prediction project. *Bull. Am. Meteorol. Soc.*, https://doi.org/10.1175/BAMS-87-4-425.

Wang, B., and G. Chen, 2017: A general theoretical framework for understanding essential dynamics of Madden–Julian oscillation. *Clim. Dyn.*, https://doi.org/10.1007/s00382-016-3448-1.

Wang, B., G. Chen, and F. Liu, 2019: Diversity of the Madden-Julian oscillation. *Sci. Adv.*, https://doi.org/10.1126/sciadv.aax0220.

Wang, B., and S. S. Lee, 2017: MJO propagation shaped by zonal asymmetric structures: Results from 24 GCM simulations. *J. Clim.*, https://doi.org/10.1175/JCLI-D-16-0873.1.

Wang, B., and Coauthors, 2018: Dynamics-oriented diagnostics for the Madden-Julian oscillation. *J. Clim.*, https://doi.org/10.1175/JCLI-D-17-0332.1.

Wang, B., F. Liu, and G. Chen, 2016: A trio-interaction theory for Madden–Julian oscillation. *Geosci. Lett.*, https://doi.org/10.1186/s40562-016-0066-z.

Wang, L., T. Li, E. Maloney, and B. Wang, 2017: Fundamental causes of propagating and nonpropagating MJOs in MJOTF/GASS models. *J. Clim.*, https://doi.org/10.1175/JCLI-D-16-0765.1.

Wang, L., T. Li, and T. Nasuno, 2018: Impact of Rossby and Kelvin wave components on MJO eastward propagation. *J. Clim.*, https://doi.org/10.1175/JCLI-D-17-0749.1.

Weaver, S. J., W. Wang, M. Chen, and A. Kumar, 2011: Representation of MJO Variability in the NCEP Climate Forecast System. *J. Clim.*, https://doi.org/10.1175/2011JCLI4188.1.

Wei, Y., and H. L. Ren, 2019: Modulation of ENSO on fast and slow MJO modes during boreal winter. *J. Clim.*, https://doi.org/10.1175/JCLI-D-19-0013.1.

Wheeler, M. C., and H. H. Hendon, 2004: An all-season real-time multivariate MJO index: Development of an index for monitoring and prediction. *Mon. Weather Rev.*, https://doi.org/10.1175/1520-0493(2004)132<1917:AARMMI>2.0.CO;2.

Wheeler, M. C., H. H. Hendon, S. Cleland, H. Meinke, and A. Donald, 2009: Impacts of the Madden-Julian oscillation on australian rainfall and circulation. *J. Clim.*, https://doi.org/10.1175/2008JCLI2595.1.

Wheeler, M., and G. N. Kiladis, 1999: Convectively Coupled Equatorial Waves: Analysis of Clouds and Temperature in the Wavenumber-Frequency Domain. *J. Atmos. Sci.*, https://doi.org/10.1175/1520-0469(1999)056<0374:CCEWAO>2.0.CO;2.

Wolding, B. O., and E. D. Maloney, 2015: Objective diagnostics and the Madden-Julian Oscillation. Part II: Application to moist static energy and moisture budgets. *J. Clim.*, https://doi.org/10.1175/JCLI-D-14-00689.1.

Wolding, B. O., E. D. Maloney, and M. Branson, 2016: Vertically resolved weak temperature gradient analysis of the Madden-Julian Oscillation in SP-CESM. *J. Adv. Model. Earth Syst.*, https://doi.org/10.1002/2016MS000724.

Wu, C. H., and H. H. Hsu, 2009: Topographic influence on the MJO in the maritime continent. *J. Clim.*, https://doi.org/10.1175/2009JCLI2825.1.

Wu, M. L. C., S. D. Schubert, M. J. Suarez, P. J. Pegion, and D. E. Waliser, 2006: Seasonality and meridional propagation of the MJO. *J. Clim.*, https://doi.org/10.1175/JCLI3680.1.

Yanai, M., S. Esbensen, and J.-H. Chu, 1973: Determination of Bulk Properties of Tropical Cloud Clusters from Large-Scale Heat and Moisture Budgets. *J. Atmos. Sci.*, https://doi.org/10.1175/1520-0469(1973)030<0611:dobpot>2.0.co;2.

Yanai, M., and R. H. Johnson, 1993: Impacts of Cumulus Convection on Thermodynamic Fields. *The Representation of Cumulus Convection in Numerical Models*.

Yoo, C., S. Lee, and S. B. Feldstein, 2012: Mechanisms of arctic surface air temperature change in response to the Madden-Julian oscillation. *J. Clim.*, https://doi.org/10.1175/JCLI-D-11-00566.1.

Yoo, C., and S. W. Son, 2016: Modulation of the boreal wintertime Madden-Julian oscillation by the stratospheric quasi-biennial oscillation. *Geophys. Res. Lett.*, https://doi.org/10.1002/2016GL067762.

Yu, J.-Y., and J. D. Neelin, 1994: Modes of Tropical Variability under Convective Adjustment and the Madden–Julian Oscillation. Part II: Numerical Results. *J. Atmos. Sci.*, https://doi.org/10.1175/1520-0469(1994)051<1895:motvuc>2.0.co;2.

Zhang, C., Á. F. Adames, B. Khouider, B. Wang, and D. Yang, 2020: FOUR THEORIES OF THE MADDEN-JULIAN OSCILLATION. *Rev. Geophys.*, https://doi.org/10.1029/2019rg000685.

Zhang, C., 2005: Madden-Julian Oscillation. *Rev. Geophys.*, https://doi.org/10.1029/2004RG000158.

Zhang, C., and J. Ling, 2017: Barrier effect of the Indo-Pacific Maritime Continent on the MJO: Perspectives from tracking MJO precipitation. *J. Clim.*, https://doi.org/10.1175/JCLI-D-16-0614.1.

Zhang, C., and B. Zhang, 2018: QBO-MJO Connection. *J. Geophys. Res. Atmos.*, https://doi.org/10.1002/2017JD028171.

Zhou, S., and A. J. Miller, 2005: The interaction of the Madden-Julian oscillation and the Arctic oscillation. *J. Clim.*, https://doi.org/10.1175/JCLI3251.1.